Monthly Notices
of the
ROYAL ASTRONOMICAL SOCIETY

MNRAS **486,** 4233–4251 (2019)
Advance Access publication 2019 April 4

doi:10.1093/mnras/stz943

# Measurement of the extragalactic background light using MAGIC and *Fermi*-LAT gamma-ray observations of blazars up to $z = 1$

MAGIC Collaboration:V. A. Acciari,[1,2] S. Ansoldi,[3] L. A. Antonelli,[4] A. Arbet Engels,[5] D. Baack,[6] A. Babić,[7] B. Banerjee,[8] U. Barres de Almeida,[9] J. A. Barrio,[10] J. Becerra González,[1,2] W. Bednarek,[11] L. Bellizzi,[12] E. Bernardini,[13,26] A. Berti,[14,27] J. Besenrieder,[15] W. Bhattacharyya,[13] C. Bigongiari,[4] A. Biland,[5] O. Blanch,[16] G. Bonnoli,[12] G. Busetto,[17] R. Carosi,[18] G. Ceribella,[15] Y. Chai,[15] S. Cikota,[7] S. M. Colak,[16] U. Colin,[15] E. Colombo,[1,2] J. L. Contreras,[10] J. Cortina,[16] S. Covino,[4] V. D'Elia,[4] P. Da Vela,[18] F. Dazzi,[4] A. De Angelis,[17] B. De Lotto,[3] M. Delfino,[16,28] J. Delgado,[16,28] F. Di Pierro,[14] E. Do Souto Espiñeira,[16] A. Domínguez,[10★] D. Dominis Prester,[7] D. Dorner,[19] M. Doro,[17] D. Elsaesser,[6] V. Fallah Ramazani,[20] A. Fattorini,[6] A. Fernández-Barral,[17] G. Ferrara,[4] D. Fidalgo,[10] L. Foffano,[17] M. V. Fonseca,[10] L. Font,[21] C. Fruck,[15] D. Galindo,[22] S. Gallozzi,[4] R. J. García López,[1,2] M. Garczarczyk,[13] S. Gasparyan,[23] M. Gaug,[21] N. Godinović,[7] D. Green,[15] D. Guberman,[16] D. Hadasch,[24] A. Hahn,[15] T. Hassan,[1,16★] J. Herrera,[1,2] J. Hoang,[10] D. Hrupec,[7] S. Inoue,[24] K. Ishio,[15] Y. Iwamura,[24] H. Kubo,[24] J. Kushida,[24] A. Lamastra,[4] D. Lelas,[7] F. Leone,[4] E. Lindfors,[20] S. Lombardi,[4] F. Longo,[3,27] M. López,[10] R. López-Coto,[17] A. López-Oramas,[1,2] B. Machado de Oliveira Fraga,[9] C. Maggio,[21] P. Majumdar,[8] M. Makariev,[25] M. Mallamaci,[17] G. Maneva,[25] M. Manganaro,[7] K. Mannheim,[19] L. Maraschi,[4] M. Mariotti,[17] M. Martínez,[16] S. Masuda,[24] D. Mazin,[15] S. Mićanović,[7] D. Miceli,[3] M. Minev,[25] J. M. Miranda,[12] R. Mirzoyan,[15] E. Molina,[22] A. Moralejo,[1,16★] D. Morcuende,[10] V. Moreno,[21] E. Moretti,[16] P. Munar-Adrover,[21] V. Neustroev,[20] A. Niedzwiecki,[11] M. Nievas Rosillo,[1,10,13★] C. Nigro,[13] K. Nilsson,[20] D. Ninci,[16] K. Nishijima,[24] K. Noda,[24] L. Nogués,[16] M. Nöthe,[6] S. Paiano,[17] J. Palacio,[16] M. Palatiello,[3] D. Paneque,[15] R. Paoletti,[12] J. M. Paredes,[22] P. Peñil,[10] M. Peresano,[3] M. Persic,[3,29] P. G. Prada Moroni,[18] E. Prandini,[17] I. Puljak,[7] W. Rhode,[6] M. Ribó,[22] J. Rico,[16] C. Righi,[4] A. Rugliancich,[18] L. Saha,[10] N. Sahakyan,[23] T. Saito,[24] K. Satalecka,[13] T. Schweizer,[15] J. Sitarek,[11] I. Šnidarić,[7] D. Sobczynska,[11] A. Somero,[1,2] A. Stamerra,[4] D. Strom,[15] M. Strzys,[15] T. Surić,[7] F. Tavecchio,[4] P. Temnikov,[25] T. Terzić,[7] M. Teshima,[15] N. Torres-Albà,[22] S. Tsujimoto,[24] J. van Scherpenberg,[15] G. Vanzo,[1,2★] M. Vázquez Acosta,[1,2★] I. Vovk,[15] M. Will[15] and D. Zarić[7]

*Affiliations are listed at the end of the paper*

Accepted 2019 March 29. Received 2019 March 21; in original form 2018 December 18

* E-mail: alberto@gae.ucm.es (AD); thassan@ifae.es (TH); moralejo@ifae.es (AM); mnievas@ucm.es (MNR); gvanzo@iac.es (GV); monicava@iac.es (MVA)

© 2019 The Author(s)
Published by Oxford University Press on behalf of the Royal Astronomical Society

Downloaded from https://academic.oup.com/mnras/article-abstract/486/3/4233/5427920 by Universita degli Studi di Pisa user on 10 April 2020

**ABSTRACT**

We present a measurement of the extragalactic background light (EBL) based on a joint likelihood analysis of 32 gamma-ray spectra for 12 blazars in the redshift range $z = 0.03$–$0.944$, obtained by the MAGIC telescopes and *Fermi*-LAT. The EBL is the part of the diffuse extragalactic radiation spanning the ultraviolet, visible, and infrared bands. Major contributors to the EBL are the light emitted by stars through the history of the Universe, and the fraction of it that was absorbed by dust in galaxies and re-emitted at longer wavelengths. The EBL can be studied indirectly through its effect on very high energy photons that are emitted by cosmic sources and absorbed via $\gamma\gamma$ interactions during their propagation across cosmological distances. We obtain estimates of the EBL density in good agreement with state-of-the-art models of the EBL production and evolution. The $1\sigma$ upper bounds, including systematic uncertainties, are between 13 per cent and 23 per cent above the nominal EBL density in the models. No anomaly in the expected transparency of the Universe to gamma-rays is observed in any range of optical depth. We also perform a wavelength-resolved EBL determination, which results in a hint of an excess of EBL in the 0.18–0.62 μm range relative to the studied models, yet compatible with them within systematics.

**Key words:** galaxies: active – gamma-rays: galaxies – infrared: diffuse background – infrared: galaxies.

## 1 INTRODUCTION

The extragalactic background light (EBL) is a cosmic diffuse radiation field that encloses essential information about galaxy evolution and cosmology (see e.g. Hauser & Dwek 2001; Domínguez & Prada 2013; Dwek & Krennrich 2013 and references therein). It is mainly composed of the ultraviolet, optical, and near-infrared light emitted by stars through the history of the Universe, possibly including light from the (yet undetected) population-III stars (e.g. Inoue et al. 2014). A fraction of these photons is absorbed by interstellar dust and re-emitted at longer wavelengths, producing the characteristic double peak spectral energy distribution of the EBL. This radiation is accumulated over the cosmic history, and redshifted by the expansion of the Universe. There may be additional contributions to the EBL, such as those connected to accretion processes on to supermassive black holes (e.g. Kormendy & Ho 2013; Shankar et al. 2016), or even more exotic sources such as products of the decay of relic dark matter particles (e.g. Murase & Beacom 2012).

The direct detection of the EBL using absolute photometry is challenging because of strong foregrounds, mainly zodiacal light but also the brightness of our own Galaxy (e.g. Arendt et al. 1998; Gorjian, Wright & Chary 2000). Therefore, attempts at direct detection are subject to large uncertainties and biases (e.g. Matsumoto et al. 2005; Bernstein 2007; Matsuoka et al. 2011; Mattila et al. 2017). Other methods focus on measuring the background anisotropies, which still provides inconclusive results (e.g. Helgason et al. 2014; Zemcov et al. 2014, 2017; Helgason & Komatsu 2017; Matsuura et al. 2017). None of these techniques provides direct information about the evolution of the EBL with cosmic redshift.

An alternative methodology to estimate the EBL is based on counting photons in different photometric bands using data from deep galaxy surveys (e.g. Madau & Pozzetti 2000; Fazio et al. 2004; Keenan et al. 2010; Tsumura et al. 2013; Driver et al. 2016). This procedure results in EBL estimates that can be considered lower limits, since light from faint undetected galaxy populations or from the outer regions of normal galaxies may be missed (e.g. Bernstein, Freedman & Madore 2002). Furthermore, cosmic variance may contribute to systematic uncertainties using this technique (Somerville et al. 2004).

Efforts centred on building models of the EBL utilize different complementary strategies. Following the classification by Domínguez et al. (2011b), these models are divided in four different classes: (1) Forward evolution models that use semi-analytical models of galaxy formation (e.g. Gilmore et al. 2012; Somerville et al. 2012; Inoue et al. 2013), (2) backward evolution models based on local or low-redshift galaxy data, which are extrapolated to higher redshifts making some assumptions on galaxy evolution (e.g. Franceschini, Rodighiero & Vaccari 2008; Franceschini & Rodighiero 2017), (3) inferred evolution from the cosmic star formation history (SFH) of the Universe (e.g. Kneiske, Mannheim & Hartmann 2002; Finke, Razzaque & Dermer 2010; Khaire & Srianand 2015; Andrews et al. 2018), and (4) observed evolution based on galaxy data over a broad range of redshift (e.g. Domínguez et al. 2011b; Helgason & Kashlinsky 2012; Stecker, Scully & Malkan 2016). Basically, these models converge to spectral intensities that are close or even match those derived from galaxy counts, at least around the shorter wavelength peak. Uncertainties are larger at the far-IR peak, since most of these models do not include data at those wavelengths, and the luminosity evolution is much faster and more difficult to trace because of source confusion and other instrument limitations (e.g. Barger, Cowie & Richards 2000; Takeuchi et al. 2001; Berta et al. 2010).

Another technique that has become rather successful to constrain the EBL is based on the observation of gamma-rays from distant extragalactic sources. This strategy relies on the fact that photons with energies larger than about 10 GeV traveling cosmological distances suffer an energy- and distance-dependent attenuation by pair-production interaction with the EBL (Nikishov 1962; Gould & Schréder 1966). In general, this technique is based on making more or less sophisticated assumptions on the intrinsic/unattenuated energy spectra of the sources, which allows, by comparison with the observed spectra, to derive information on the EBL and, very importantly, on its evolution. Early attempts provided upper limits on the background intensity (e.g. Stecker, de Jager & Salamon 1992; Aharonian et al. 2006; Mazin & Raue 2007; Meyer et al. 2012). Yet, more recently, thanks to the availability of more and better gamma-ray data, the EBL detection has been claimed by different groups (Ackermann et al. 2012; Abramowski et al. 2013;



Downloaded from https://academic.oup.com/mnras/article-abstract/486/3/4233/5427920 by Universita degli Studi di Pisa user on 10 April 2020

**Table 1.** Summary of the 32 MAGIC spectra used in the determination of the EBL density. The sample includes flat spectrum radio quasars (FSRQs), and intermediate- and high-frequency-peaked BL Lac objects (IBLs and HBLs, respectively) – see e.g. Ghisellini et al. (2011). The redshift of PG 1553+113 is only approximately known; the quoted estimated range is from Danforth et al. (2010).

| Source | Blazar type | Redshift | Observational period | Obs. $t$ (h) |
|---|---|---|---|---|
| Markarian 421 (15 data sets) | HBL | 0.030 | 2013.04.10–19, 2014.04.26 | 43.8 |
| 1ES 1959+650 | HBL | 0.048 | 2015.11.06–18 | 4.8 |
| 1ES 1727+502 | HBL | 0.055 | 2015.10.12–2015.11.02 | 6.4 |
| BL Lacertae | IBL | 0.069 | 2015.06.15 | 1.0 |
| 1ES 0229+200 | HBL | 0.14 | 2012–2015 | 105.2 |
| 1ES 1011+496 | HBL | 0.212 | 2014.02.06–2014.03.07 | 11.8 |
| PKS 1510−089 (2 data sets) | FSRQ | 0.361 | 2015.05.18–19, 2016.05.31 | 5.0 |
| PKS 1222+216 | FSRQ | 0.432 | 2010.06.18 | 0.5 |
| PG 1553+113 (5 data sets) | HBL | 0.43–0.58 | 2012–2016 | 66.4 |
| PKS 1424+240 (2 data sets) | HBL | 0.604 | 2014, 2015 | 49.1 |
| PKS 1441+25 | FSRQ | 0.939 | 2015.04.18–23 | 20.1 |
| QSO B0218+35 | FSRQ | 0.944 | 2014.07.25–26 | 2.1 |
| Total | | | | 316.1 |

Domínguez et al. 2013; Biteau & Williams 2015; Ahnen et al. 2016a; Abdalla et al. 2017; Abdollahi et al. 2018). These EBL detections constrain the background intensities to be close to the lower limits provided by galaxy counts (within a factor of 2 or smaller, depending on the energy). However, they are in strong tension with those intensities obtained from early direct detection attempts such as the one presented by Matsumoto et al. (2005), Matsumoto et al. (2015), and Bernstein (2007), yet still compatible, or slightly in tension, with more recent estimates such as those by Matsuoka et al. (2011), Matsuura et al. (2017), and Mattila et al. (2017).

Although great progress has been achieved in the study of the EBL in the past years, more work is definitely necessary, particularly in the study of EBL evolution and its high-redshift properties. Interestingly, in the last years, the MAGIC imaging atmospheric Cherenkov telescopes (IACTs) have detected the two farthest sources to date in the very high energy (VHE) band, both of them at $z \sim 1$ (Ahnen et al. 2015, 2016b). These detections significantly expand the redshift range of sources available for gamma-ray attenuation measurements from the ground.

In this paper, we present EBL constraints based on a joint likelihood analysis of 12 blazars observed with MAGIC during extensive campaigns totalling over 300 h of exposure, including observations of the most distant VHE sources detected. Additionally, we add lower energy data (from 0.1 to $\simeq$100 GeV) taken by the Large Area Telescope (LAT) on-board the *Fermi Gamma-ray Space Telescope* during similar time ranges as the MAGIC observations. The combination of contemporaneous MAGIC and LAT data allows us to have a better estimate of the intrinsic spectral energy distribution of a given blazar, since the energy range covered by LAT is only slightly affected by absorption in the EBL.

This paper is organized as follows. Section 2 describes the MAGIC and *Fermi*-LAT data sets, including the data selection and the analysis methods for both instruments. In Section 3, we introduce the proposed methodology to measure the EBL density assuming different EBL template models, and present the results, both for the full sample and for four sub-samples defined by source redshift. This section describes also the systematic uncertainties of the method. Section 4 presents a wavelength-resolved estimate of the EBL density. Finally, in Section 5 we summarize the main results of this study, and Appendix A provides technical details of the analysis method used throughout the paper.

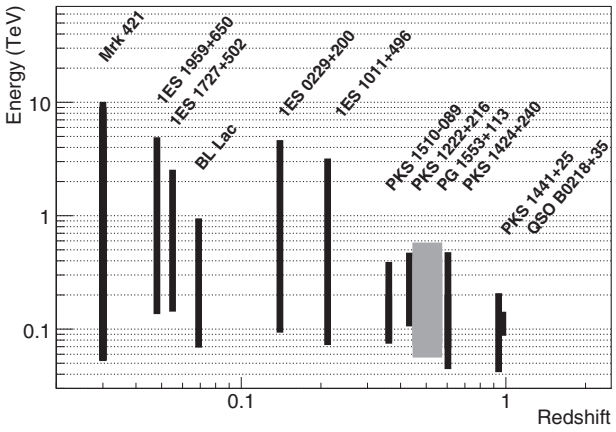


**Figure 1.** Summary of the MAGIC data sample: energy range probed by the observations versus source redshift.

## 2 DATA SAMPLE

A large majority of the known extragalactic VHE sources are blazars, a class of active galactic nuclei with jets closely aligned with the line of sight of the observer (Urry & Padovani 1995). For this study, we have selected 32 VHE spectra from 12 blazars, obtained with MAGIC in the period June 2010 to May 2016, with a total observation time (after quality cuts) of 316 h. The sources span the range 0.030–0.944 in redshift, and the sample includes both multiyear observations of persistent sources (1ES 0229+200, PG 1553+113, PKS 1424+240) and target of opportunity observations of flaring sources (on time-scales from less than 1 h to around 1 month). Table 1 lists the 12 sources and provides the basic parameters of the observations. Fig. 1 shows the energy range of the MAGIC observations for each source, plotted versus the source redshift.

### 2.1 MAGIC observations

MAGIC is a system of two IACTs located at the Roque de los Muchachos Observatory on the island of La Palma in Spain (Aleksić et al. 2016a). Equipped with 17 m diameter mirror dishes and fast, 1039-pixel PMT cameras, the telescopes record images of extensive air showers in stereoscopic mode, enabling the observation of VHE gamma-ray sources at energies $\gtrsim$50 GeV. The data analysis is performed using the standard MAGIC analysis and reconstruction software MARS (Zanin et al. 2013; Aleksić et al. 2016b). All data used for this study were taken during dark nights in good weather conditions. Atmospheric transmission was monitored with the MAGIC LIDAR (Fruck et al. 2013). After data quality cuts, the median of the aerosol transparency measurements within each of the 32 samples in Table 1, relative to that of an optimal night, ranges between 0.9 and 1.0, except for the case of the observations of PKS 1510−089 on 2015 May, for which it is 0.83 (this is the only sample

Downloaded from https://academic.oup.com/mnras/article-abstract/486/3/4233/5427920 by Universita degli Studi di Pisa user on 10 April 2020

for which a correction for atmospheric transmission, based on the LIDAR data, had to be applied).

After selection of pixels with a significant signal in each of the cameras, a set of parameters describing the images is calculated (among which are the well-known Hillas parameters; Hillas 1985). The stereoscopic reconstruction of the geometry of the shower is then performed, using the parameters from both images, to obtain its direction and location relative to the telescopes. The energy of the primary is estimated, assuming a purely electromagnetic shower, using look-up tables that make use of all relevant parameters. This method allows us to achieve a relative energy resolution between 15 and 23 per cent depending on the energy (Aleksić et al. 2016b). The random forest method (Breiman 2001), fed with image parameters, is then used to obtain a refined estimate of the shower direction, and to tag events with a test statistic for particle identification dubbed *hadronness* (Albert et al. 2008). Energy-dependent cuts in *hadronness*, and in the angular distance between the target source and the reconstructed event direction, are then applied to improve the signal-to-noise ratio of the data before obtaining the VHE gamma-ray spectrum of the observed source. In the process outlined above, the energy look-up tables and random forests are created using a training sample of Monte Carlo (MC) simulated gamma-ray initiated showers (using version 6.500 of the CORSIKA program, Heck et al. 1998, and a detailed simulation of the optics and electronics of the telescopes). For the training of the event-tagging random forest, a sample of hadronic-shower-dominated real MAGIC data from off-source observations is used together with the gamma MC. An independent sample of MC gamma events is processed in the same way as the real data to obtain the instrument response functions (IRFs; effective area and energy migration matrix) needed for the spectral analysis of the sources. Since the data span multiple years and the performance of MAGIC has changed over time, several independent MC libraries (tuned to the MAGIC performance in independent periods lasting from few months to over one year) were used in the analysis.

### 2.2 *Fermi*-LAT observations

The *Fermi*-LAT (Atwood et al. 2009) is a pair conversion detector consisting of a 4 × 4 array of silicon strip trackers and tungsten converters and a cesium iodide (CsI) based calorimeter. The instrument is fully covered by a segmented anticoincidence shield that provides a highly efficient vetoing against charged particle background events. The LAT is sensitive to gamma-rays from 20 MeV to more than 300 GeV. It normally operates in survey mode, covering the whole sky every 3 h and providing an instantaneous field of view of 2.4 sr (i.e. 20 per cent of the sky).

The *Fermi*-LAT data were extracted from the weekly LAT data files available at the FSSC data centre.[1] For each data sample, we consider only Pass-8 source-class photons detected in a *region of interest* (ROI) of 15° radius centred on the nominal position of the analysed source. Only events whose estimated energy lies between 100 MeV and 500 GeV were selected. Following the event selection recommendations from the *Fermi*-LAT analysis *Cicerone*,[2] we only included good data [`(DATA_QUAL>0)&&(LAT_CONFIG==1)`] with zenith distance lower than 90°. The time-based filtering of the data was done to balance out photon statistics and systematic uncertainties arising from the lack of strict simultaneity with respect to the MAGIC observations. By default, we selected events from 12:00 UTC (noon) of the day preceding the first VHE observations until 12:00 UTC of the day following the last night in which VHE data were taken, ensuring that at least 24 h of LAT data are included in the analysis. For very fast flares with enough photon statistics in high-energy gamma-rays, we further restricted the time intervals to ensure that MAGIC and *Fermi*-LAT data corresponded approximately to the same level of activity of the source. This included 3.6 h centred around the two MAGIC observations of PKS 1510−089 in 2015, 6 h centred around the MAGIC observations of PKS 1222+21, 8 h and 7 h centred around the MAGIC observations of Mrk 421 on 2013 April 11 and April 15, respectively. For the two highest flux nights during the 2013 April Mrk421 flare (20130413 and 20130415), the MAGIC observations were split into three sub-samples (a,b,c), each of $\simeq$ 2 h duration, according to their flux level. The signal in the LAT observations was however not high enough to provide independent spectra for each of those sub-periods, and hence a single LAT spectrum has been computed for each night. It must be noted that, while the gamma-ray flux measured by MAGIC on those nights is highly variable (by up to a factor 2) in the TeV range, it is stable within uncertainties around 100 GeV, so all three MAGIC spectra of each night connect smoothly with the corresponding average LAT spectrum.

The case of 1ES 0229+200 also demanded a special treatment. The source is an extreme HBL BL Lac that required the integration of a much larger LAT exposure, of more than 6 yr, in order to provide a reasonable detection, TS $\sim$ 80. TS is a Test Statistic for source detection defined in terms of a likelihood ratio test (LRT) as TS = $-2\log(L_{\mathrm{max,\,H0}}/L_{\mathrm{max,H1}})$, where H0 is the null hypothesis, obtained by removing the source of interest from the source model that was generated for H1 (Mattox et al. 1996). Finally, for 1ES 1011+496, *Fermi*-LAT observations were optimized to account for the MAGIC Moon break, hence including only data from 2012 February 5 to February 12 and then February 21 until March 7.

The full list of *Fermi*-LAT observations is shown in Table 2. Two examples of SEDs obtained in contemporaneous MAGIC and LAT observations for Mrk 421 and PG 1553+113 are shown in Fig. 2. For each data sample, the data were reduced and analysed using the open-source software package ENRICO (Sanchez & Deil 2013) as a wrapper for the *Fermi* SCIENCETOOLS (version v10r0p5).[3] We followed a binned likelihood analysis approach split in PSF event types (0, 1, 2, and 3) with 10 bins per energy decade and using the IRFs P8R2_SOURCE_V6. All the 3FGL (third *Fermi*-LAT source catalogue; Acero et al. 2015) sources within the ROI are included in the model, along with Galactic and isotropic models using `gll_iem_v06.fits` and `iso_P8R2_SOURCE_V6_v06.txt` files, respectively. The spectral model used for each of the sources was selected in order to maximize $L_{\mathrm{max,H1}}$. With the exception of 1ES 0229+200, for which a pure power law was the model of choice, the rest of the data samples were modelled using curved spectral shapes, either by allowing EBL absorption to have an effect at the highest energies or by using models with intrinsic curvature terms [log parabola (LP) and power law with exponential cut-off]. The spectral parameters of all sources with TS > 4 within a radius of 3° around the source of interest were left free in the likelihood maximization. The parameters of the rest of the sources are fixed to the published 3FGL values. We also left free the normalization of the diffuse components. Finally, the data

[1] https://fermi.gsfc.nasa.gov/ssc/data/access/

[2] https://fermi.gsfc.nasa.gov/ssc/data/analysis/documentation/Cicerone/

[3] http://fermi.gsfc.nasa.gov/ssc/data/analysis/scitools



Downloaded from https://academic.oup.com/mnras/article-abstract/486/3/4233/5427920 by Universita degli Studi di Pisa user on 10 April 2020

**Table 2.** List of observations selected in *Fermi*-LAT. Period stands for the corresponding MAGIC observation. For 1ES 0229+200, *all* means that all the data available from the *Fermi*-LAT was integrated. For PG 1553+113, the periods dubbed ST0X0Y group data taken in periods of stable MAGIC performance and IRFs, where X denotes major hardware changes and Y refers to minor changes. They correspond to the five data sets introduced in Table 1. TSTART and TSTOP denote the limits of the *Fermi*-LAT integration periods. Note that for some sources, periods within these limits for which no MAGIC observations exist have been excluded. The quoted *Redshift* and Analysis *Model* are those used in fitting the *Fermi*-LAT data of the given source, from which the bow-ties later used in the EBL constraints are obtained. Finally, *TS* denotes the Test Statistics, related to the statistical significance of the source detection.

| Source [period] | Redshift | TSTART | TSTOP | Exposure (d) | Model | TS |
|---|---|---|---|---|---|---|
| 1ES 0229+200 [all] | 0.14 | 2009-11-01T00:00 | 2017-01-01T12:00 | 2200 | PWL | 113 |
| 1ES 1011+496 [2014] | 0.212 | 2014-02-05T12:00 | 2014-03-07T12:00 | 17.7 | EPWL | 426 |
| 1ES 1727+502 [2015] | 0.055 | 2015-03-29T12:00 | 2015-11-02T12:00 | 57.3 | PWL | 98 |
| 1ES 1959+650 [2015] | 0.047 | 2015-11-05T12:00 | 2015-11-18T12:00 | 11 | LP | 405 |
| B 0218+357 [2014] | 0.944 | 2014-07-24T21:00 | 2014-07-26T12:00 | 1.37 | PWL | 179 |
| BL Lac [20150615] | 0.069 | 2015-06-14T15:00 | 2015-06-15T03:00 | 0.376 | PWL | 26 |
| Mrk 421 [20130410] | 0.03 | 2013-04-09T12:00 | 2013-04-10T12:00 | 0.845 | PWL | 179 |
| Mrk 421 [20130411] | 0.03 | 2013-04-10T18:00 | 2013-04-11T06:00 | 0.389 | PWL | 44 |
| Mrk 421 [20130412] | 0.03 | 2013-04-11T18:00 | 2013-04-12T06:00 | 0.388 | PWL | 120 |
| Mrk 421 [20130413a] | 0.03 | 2013-04-12T12:00 | 2013-04-13T12:00 | 0.848 | PWL | 158 |
| Mrk 421 [20130413b] | 0.03 | 2013-04-12T12:00 | 2013-04-13T12:00 | 0.848 | PWL | 158 |
| Mrk 421 [20130413c] | 0.03 | 2013-04-12T12:00 | 2013-04-13T12:00 | 0.848 | PWL | 158 |
| Mrk 421 [20130414] | 0.03 | 2013-04-13T12:00 | 2013-04-14T12:00 | 0.844 | PWL | 122 |
| Mrk 421 [20130415a] | 0.03 | 2013-04-14T21:17 | 2013-04-15T04:13 | 0.209 | PWL | 81 |
| Mrk 421 [20130415b] | 0.03 | 2013-04-14T21:17 | 2013-04-15T04:13 | 0.209 | PWL | 81 |
| Mrk 421 [20130415c] | 0.03 | 2013-04-14T21:17 | 2013-04-15T04:13 | 0.209 | PWL | 81 |
| Mrk 421 [20130416] | 0.03 | 2013-04-15T12:00 | 2013-04-16T09:00 | 0.723 | PWL | 110 |
| Mrk 421 [20130417] | 0.03 | 2013-04-16T18:00 | 2013-04-17T06:00 | 0.359 | PWL | 23 |
| Mrk 421 [20130418] | 0.03 | 2013-04-17T12:00 | 2013-04-18T12:00 | 0.845 | PWL | 87 |
| Mrk 421 [20130419] | 0.03 | 2013-04-18T12:00 | 2013-04-19T12:00 | 0.844 | PWL | 104 |
| Mrk 421 [2014] | 0.03 | 2014-04-25T18:00 | 2014-04-26T06:00 | 0.365 | PWL | 69 |
| PG 1553+113 [ST0202] | 0.45 | 2012-02-28T12:00 | 2012-03-04T12:00 | 4.22 | PWL | 71 |
| PG 1553+113 [ST0203] | 0.45 | 2012-03-13T12:00 | 2012-05-02T12:00 | 41.9 | PWL | 457 |
| PG 1553+113 [ST0302] | 0.45 | 2013-04-07T12:00 | 2013-06-12T12:00 | 55.7 | LP | 475 |
| PG 1553+113 [ST0303] | 0.45 | 2014-03-11T12:00 | 2014-03-25T12:00 | 11.8 | PWL | 207 |
| PG 1553+113 [ST0306] | 0.45 | 2015-01-25T12:00 | 2015-08-07T12:00 | 164 | EPWL | 2606 |
| PKS 1222+216 [2010] | 0.432 | 2010-06-17T20:00 | 2010-06-18T00:00 | 0.152 | LP | 224 |
| PKS 1424+240 [2014] | 0.6 | 2014-03-23T12:00 | 2014-06-18T12:00 | 73.3 | PWL | 453 |
| PKS 1424+240 [2015] | 0.6 | 2015-01-22T12:00 | 2015-06-13T12:00 | 120 | PWL | 945 |
| PKS 1441+25 [2015] | 0.94 | 2015-04-17T12:00 | 2015-04-23T12:00 | 5.06 | PWL | 621 |
| PKS 1510−089 [2015] | 0.36 | 2015-05-17T22:48 | 2015-05-19T02:10 | 0.299 | EPWL | 369 |
| PKS 1510−089 [2016] | 0.36 | 2016-05-30T12:00 | 2016-05-31T12:00 | 0.843 | EPWL | 204 |

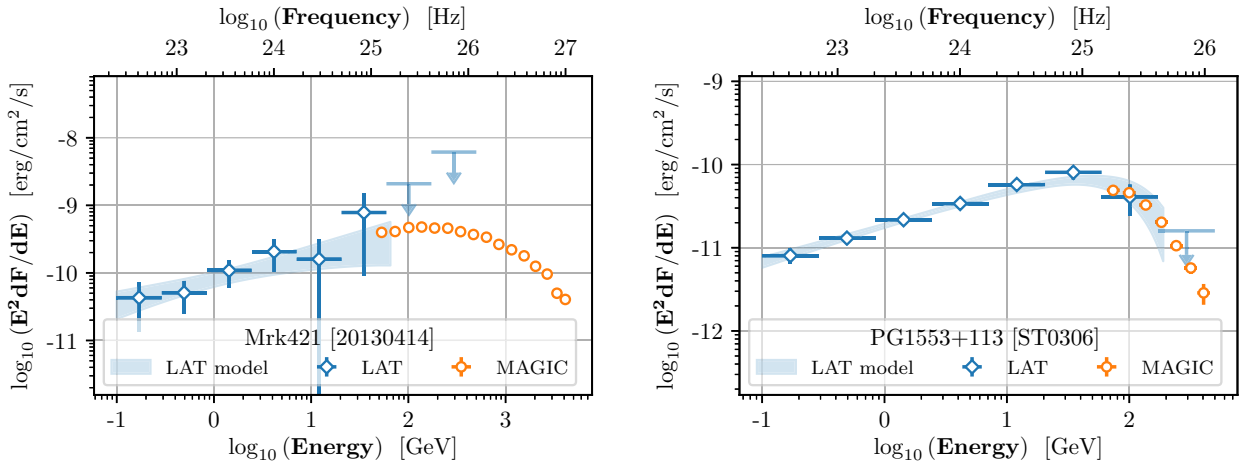


**Figure 2.** Detailed broad-band gamma-ray spectral energy distributions of the Markarian 421 data set of 2013 April 14 (short exposure) and the ST0306 2015 data from PG 1553+113 (long integration time), showing the good level of agreement achieved for both the MAGIC spectral points (orange open points) and the HE bow-ties and spectral points obtained through the maximum likelihood analysis of *Fermi*-LAT data (blue). The *y*-axes correspond to *observed* fluxes, i.e. they include the effect of absorption by the EBL. LAT upper limits are for $2\sigma$ confidence level.

Downloaded from https://academic.oup.com/mnras/article-abstract/486/3/4233/5427920 by Universita degli Studi di Pisa user on 10 April 2020

were divided in several energy bins to obtain *Fermi*-LAT spectral points. The results were found to be in good agreement with those of MAGIC in the overlapping energy range (two examples are shown in Fig. 2. Note that the spectral shapes used for the *Fermi*-LAT analysis described above, and reported in the 'model' column of Table 2, were chosen based on the LAT data alone ($E_\gamma \lesssim 100$ GeV). They should not be confused with the spectral models used later for the joint analysis of *Fermi*-LAT and MAGIC data over a wider energy range (see Section 3.2).

## 3 CONSTRAINTS ON THE EBL DENSITY

In order to set constraints on the EBL from the observed gamma-ray spectra, we have adopted a maximum likelihood approach similar to that used in Abramowski et al. (2013). We fit simultaneously the 32 spectra in our sample, and use the profile likelihood approach to set constraints on one or more free EBL parameters. In the simplest case, a single EBL parameter $\alpha$ is used to scale the optical depth $\tau(E, z)$ from a given template EBL model. We calculate $\tau(E, z)$ from the evolving spectral photon densities provided by the EBL model using equation (1),

$$\tau(E, z) = c \int_0^z \left|\frac{\mathrm{d}t}{\mathrm{d}z'}\right| \mathrm{d}z' \int_0^2 \frac{\mu}{2} \mathrm{d}\mu \int_{\varepsilon_{\rm th}}^{\infty} \sigma(\varepsilon, E', \mu)\, n(\varepsilon, z')\, \mathrm{d}\varepsilon, \quad (1)$$

where $\mu = 1 - \cos\theta$, with $\theta$ the angle of interaction between the gamma-ray and the EBL photon, and $E' = E(1 + z')$ and $\varepsilon$ are their respective energies. The term $|\mathrm{d}t/\mathrm{d}z'|$ incorporates the $\Lambda$CDM cosmological model, $|\mathrm{d}t/\mathrm{d}z'|^{-1} = H_0\,(1 + z')\,\sqrt{\Omega_m (1 + z')^3 + \Omega_\Lambda}$, for which we adopted $H_0 = 70\ \mathrm{km\,s^{-1}\,Mpc^{-1}}$, $\Omega_m = 0.3$, and $\Omega_\Lambda = 0.7$. The factor $n(\epsilon, z')$ is the proper number density of EBL photons per unit energy. Finally, $\varepsilon_{\rm th}$ is the EBL photon energy threshold for the pair production process, $\varepsilon_{\rm th} = 2m_e^2c^4/(\mu\ E')$, and $\sigma(\varepsilon, E', \mu)$ is the cross-section of the process (Heitler 1984).

The absorption of VHE photons can be described by a term $e^{-\alpha\tau(E,\,z)}$, which depends on the energy $E$ of the gamma-rays and the redshift $z$ of the source. The spectrum of gamma-rays arriving at Earth from the source can then be written as $\mathrm{d}F/\mathrm{d}E = (\mathrm{d}F/\mathrm{d}E)_{\rm intrinsic}\, e^{-\alpha\tau(E,\,z)}$. The spectrum is then folded with the MAGIC IRFs (effective area and energy migration matrix) derived from MC simulations, and multiplied by the effective observation time, to obtain the expected number of detected gamma-ray events as a function of the estimated energy. These values and the actually observed numbers of events in bins of estimated energy are then used to build a poissonian likelihood $L$, which is maximized with $\alpha$ as a free parameter. The parameters describing the intrinsic spectra $(\mathrm{d}F/\mathrm{d}E)_{\rm intrinsic}$ are treated as nuisance parameters. Note that, by scaling $\tau$ by an overall factor $\alpha$ for all $(E, z)$ values, we implicitly assume that both the EBL evolution and spectrum are the ones in the reference model – represented by $n(\varepsilon, z')$ in equation (1). The formulation of the likelihood $L$ and other technical details of the procedure are explained in Appendix A.

### 3.1 Maximization of the likelihood

The value of the likelihood $L$ is maximized, or rather, $-2\log L$ minimized, using the MIGRAD algorithm of ROOT's MINUIT2 package (Brun & Rademakers 1997; Hatlo et al. 2005). If the maximum achieved likelihood in the space of free parameters is $L_{\rm max}$, in the asymptotic limit, the quantity $-2\log(L_{\rm max}/L*)$ is distributed as a $\chi^2$ with the number of degrees of freedom of the problem (the number of fitted $E_{\rm est}$ bins minus the number of free parameters), with $L*$ being the maximum (unconstrained) possible value of the likelihood, that of a model which predicts exactly the number of recorded ON-source and OFF-source events in every bin of estimated energy. From this $\chi^2$ we can therefore obtain the $p$-value of the fit.

The profile likelihood of the $\alpha$ parameter, $L(\alpha)$, allows us to obtain the value $\alpha_{\rm best}$ for which $L$ is maximized, to which we will refer as the 'best-fitting' EBL scale. The optical depth $\tau$ scales linearly with the EBL density, which means that $\alpha_{\rm best}$ is also the best-fitting EBL density, relative to that of the model. The method can also be interpreted as an LRT between two competing models. In the null hypothesis, the EBL density is fixed to the one in the model, i.e. $\alpha = 1$. The alternative hypothesis has $\alpha$ as an additional free parameter. According to Wilks theorem (Wilks 1938), in the asymptotic limit the test statistic $-2\log\Lambda = -2\log(L(\alpha = 1)/L(\alpha_{\rm best}))$ is distributed as a $\chi^2$ with one degree of freedom. This theorem allows us to obtain the $1\,\sigma$ uncertainties in $\alpha_{\rm best}$ as the shifts $(\Delta\alpha_+, \Delta\alpha_-)$ from $\alpha_{\rm best}$ that result in $\Delta(-\,2\log\Lambda) = 1$.

### 3.2 Choice of intrinsic spectral models

An obvious drawback of the method outlined above is the lack of certainty about the intrinsic spectral shapes, $(\mathrm{d}F/\mathrm{d}E)_{\rm intrinsic}$ of the observed sources. We assume, following authors like Mazin & Raue (2007), Abramowski et al. (2013), and Biteau & Williams (2015), that the intrinsic blazar spectra can be described by simple, smooth concave functions with three or four parameters: power law with exponential or sub/superexponential cut-off (EPWL, SEPWL), LP, and LP with exponential cut-off (ELP). Some parameters are limited so that the functions are always concave in the $\log(\mathrm{d}F/\mathrm{d}E)$ versus $\log(E)$ representation, i.e. the spectra *cannot* become harder for increasing energy. A simple power-law function (PWL, two parameters) is also considered as an option, but only for the purpose of estimating the systematic uncertainties (see Section 3.4), since it biases the results towards too high $\alpha$ values (if the intrinsic spectrum is actually concave). The functional expressions for the differential spectra, $\mathrm{d}F/\mathrm{d}E$, are the following:

PWL: $F_0\,(E/E_0)^{-\Gamma}$, EPWL: $F_0\,(E/E_0)^{-\Gamma}\,e^{-E/E_c}$,

LP: $F_0\,(E/E_0)^{-\Gamma - b\log(E/E_0)}$,

ELP: $F_0\,(E/E_0)^{-\Gamma - b\log(E/E_0)}\,e^{-E/E_c}$,

SEPWL: $F_0\,(E/E_0)^{-\Gamma}\,e^{-(E/E_c)^d}$,

where $E_0$ is a normalization energy and $F_0$, $\Gamma$, $E_c$, $b$, and $d$ are free parameters.

For a given template EBL model, we scan the values of the scaling factor $\alpha$ between 0 and 2.5 (in steps of 0.05). In each step we try, for each of the spectra, four different intrinsic spectral models: EPWL, LP, ELP, and SEPWL. This means that for every spectrum and function we make a likelihood maximization as described in Section 3.1, and obtain fit $p$-values, which allow us to compare how well the different functions describe the data for the given EBL level. We choose the function that provides the best fit (largest $p$-value) anywhere in the full scanned range of $\alpha$. Alternative selection criteria, such as the one based on the minimization of the Akaike information criterion (AIC; Akaike 1974), have also been tested and yield similar results. In some cases, LP and EPWL, which have the same number of free parameters, have exactly the same maximum $p$-value. This occurs when they happen to be degenerate with their common *parent function*, a power law. In such cases, we adopt a conservative approach: we choose the function that results in a



Downloaded from https://academic.oup.com/mnras/article-abstract/486/3/4233/5427920 by Universita degli Studi di Pisa user on 10 April 2020

**Table 3.** EBL density constraints (best-fitting EBL scale factor $\alpha_{\rm best}$) using MAGIC and MAGIC + *Fermi*-LAT spectra.

| EBL template | MAGIC-only analysis | | | MAGIC + *Fermi*-LAT analysis | | |
|---|---|---|---|---|---|---|
| | Best-fitting scale $\alpha_{\rm best}$ (stat-only) | $\chi^2$/ndf | $p$-value | Best-fitting scale (stat-only) | $\chi^2$/ndf | $p$-value |
| D11 Domínguez et al. (2011b) | 0.92 (+0.11, −0.12) | 481/415 | $1.37 \times 10^{-2}$ | 1.00 (+0.07, −0.07) | 575/469 | $5.88 \times 10^{-4}$ |
| Fi10 Finke et al. (2010) | 0.96 (+0.10, −0.12) | 488/416 | $0.83 \times 10^{-2}$ | 1.00 (+0.07, −0.08) | 581/472 | $4.43 \times 10^{-4}$ |
| F08 Franceschini et al. (2008) | 0.99 (+0.11, −0.12) | 480/415 | $1.50 \times 10^{-2}$ | 1.04 (+0.08, −0.08) | 573/469 | $7.34 \times 10^{-4}$ |
| G12 Gilmore et al. (2012) (fiducial) | 0.97 (+0.11, −0.12) | 479/414 | $1.49 \times 10^{-2}$ | 1.03 (+0.08, −0.08) | 568/471 | $1.36 \times 10^{-3}$ |
| H12 Helgason & Kashlinsky (2012) | 1.24 (+0.11, −0.16) | 492/417 | $0.68 \times 10^{-2}$ | 1.21 (+0.09, −0.10) | 582/470 | $3.12 \times 10^{-4}$ |
| I13 Inoue et al. (2013) | 0.82 (+0.13, −0.13) | 486/414 | $0.81 \times 10^{-2}$ | 1.04 (+0.11, −0.10) | 595/468 | $0.61 \times 10^{-4}$ |
| S16 Stecker et al. (2016) | 1.33 (+0.15, −0.16) | 479/414 | $1.47 \times 10^{-2}$ | 1.38 (+0.11, −0.10) | 569/472 | $1.46 \times 10^{-3}$ |
| K10 Kneiske & Dole (2010) (minimum EBL) | 1.23 (+0.14, −0.15) | 478/415 | $1.69 \times 10^{-2}$ | 1.31 (+0.09, −0.11) | 566/471 | $1.76 \times 10^{-3}$ |

flatter likelihood curve for $\alpha$, i.e. the one that is most degenerate with the effect of the EBL on the spectrum. In other words, since we assume that either of the two functions is a possible model of the intrinsic spectrum, we choose the one that constrains the EBL *less*. It must be noted that other concave functions, not considered by us, could provide an even flatter likelihood and hence a weaker EBL constraint – this underlines the fact that our EBL constraints necessarily rely on the *assumption* that the tested spectral models are good enough to describe the intrinsic spectra.

A first set of intrinsic spectral models is determined following the method just described, and are used to obtain a *preliminary* maximum likelihood estimator of the EBL scale $\alpha_{\rm best,0}(+\Delta\alpha_+, -\Delta\alpha_-)$ using all 32 spectra in the sample. A revision of the spectral model selection is then performed following a self-consistent approach, in case of spectra, if any, for which the maximum $p$-value was found for an $\alpha$ value outside the range $(\alpha_{\rm best,0} - 2\Delta\alpha_-, \alpha_{\rm best,0} + 2\Delta\alpha_+)$. In such cases, the function selection is re-done, this time comparing the $p$-values in the restricted $2\sigma$ range around $\alpha_{\rm best,0}$. Then the profile likelihood of $\alpha$ is recalculated with the revised set of spectral models, and the final estimate of $\alpha_{\rm best}$ is obtained. This model revision procedure improves (by construction) the $p$-value of the global fit.

### 3.3 Results

The method has been applied both to the MAGIC data alone, and to a combination of the MAGIC data and the *Fermi*-LAT data (the latter in the form of spectral *bow-ties*, i.e. flux and photon index at a given energy, with their respective uncertainties) that help constrain the intrinsic spectral parameters of the sources, as explained in Appendix A2. The analysis was repeated for eight different template EBL models – see Table 3 for the references and correspondence to the short names we will use to refer to them. The spectral energy distribution of the EBL (at $z = 0$) between 0.1 and 30 μm according to the eight models is shown on the top panel of Fig. 3. We think that these eight models are a good representation of the state of the art in EBL research. They span the whole range of four categories (or methodologies) described in the Introduction, i.e. (1) forward evolution, (2) backward evolution, (3) inferred evolution, (4) observed evolution.

Fig. 4 shows the profile likelihood curves from which the best-fitting EBL scale factors have been obtained for the case of the Domínguez et al. (2011b) model (hereafter, D11). Table 3 presents the best-fitting scale factors for each of the EBL templates, and the associated statistical uncertainties. Note that, as expected, the uncertainties are smaller when the *Fermi*-LAT data are included

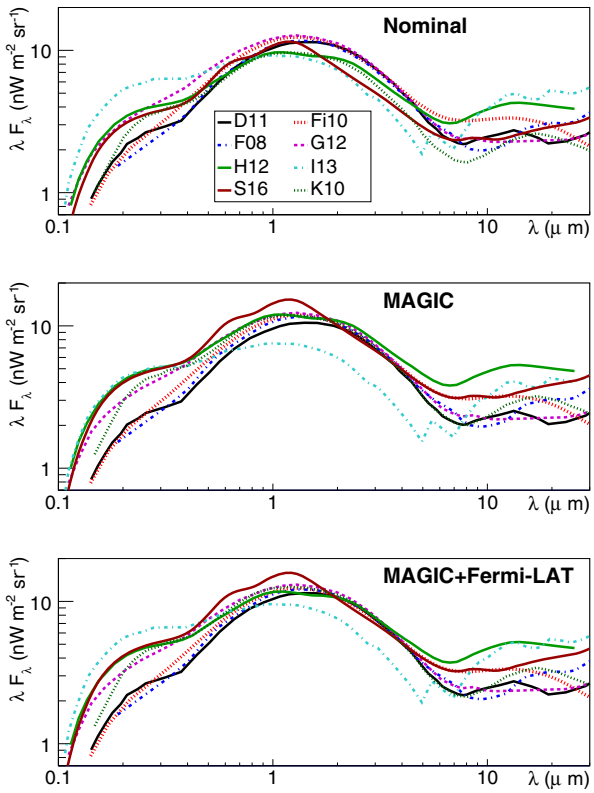


**Figure 3.** Top panel: SEDs of EBL template models used in this work, see Table 3. Middle and bottom panels: the same EBL SEDs scaled by the best-fitting EBL scale factors obtained through the analysis of MAGIC-only and MAGIC + *Fermi*-LAT data, respectively.

in the analysis. This improvement comes together with a stronger assumption on the intrinsic source spectra, namely that they are well represented by the simple concave functions listed in Section 3.2 over a wider energy range, spanning both the *Fermi*-LAT and MAGIC bands. In particular, this has an effect on the estimated $p$-values, which are around 20 times smaller when *Fermi*-LAT data are included. It should be remarked that the small $p$-values in Table 3 (all of them smaller than 0.02) are not surprising, given that (i) the method assumes no uncertainties in the energy- and redshift-dependence of the optical depths from the template EBL model; (ii) the true underlying spectra of the sources may be more complex that the used models; and (iii) no instrumental systematic uncertainties are yet considered – they are treated separately in Section 3.4.

Downloaded from https://academic.oup.com/mnras/article-abstract/486/3/4233/5427920 by Universita degli Studi di Pisa user on 10 April 2020

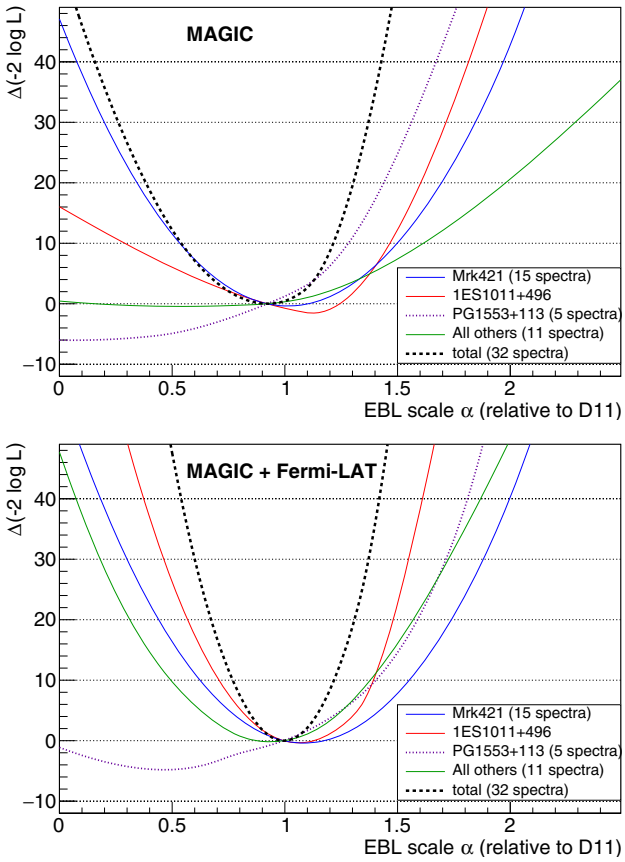


**Figure 4.** Profile likelihood of the EBL scale relative to the D11 template, for the joint analysis of 32 spectra (dashed black curves) using MAGIC-only and MAGIC + *Fermi*-LAT data. The coloured curves are the profile likelihoods obtained with subsets of the 32 spectra.

Despite these caveats, a reasonable agreement between the MAGIC and LAT spectra is achieved for all the analysed samples, as can be seen in Fig. 5.

For half of the tested EBL models (D11, Fi10, F08, and G12) the best-fitting scale factors are compatible with 1.0 within $1\sigma$, meaning that our data are compatible with the EBL density in the models. Even considering only the statistical uncertainties, the data do not allow to discriminate among the four EBL models. The other four templates (H12, I13, S16, and K10) result in scale factors that are between 1.4 and $2.2\sigma$ away from $\alpha = 1.0$ for the MAGIC-only analysis (and between 2.3 and $3.5\sigma$ for the analysis including *Fermi*-LAT, with the only exception of I13, in which the best-fitting is compatible with the EBL density in the model – though it also has the worst $p$-value of the whole set). It must be remarked that the K10 model accounts only for the contribution to the EBL of resolved sources, and is presented by their authors as a 'minimal' EBL model in the optical and near-infrared bands, the spectral range to which our gamma-ray data is most sensitive. It is therefore natural that for such a model a best-fitting scale larger than one is obtained. Likewise, the H12 model is based on measurements only up to 24 μm, so we can expect it to underestimate the total optical depth for the highest energy observations in our sample – which in turn results in a best-fitting scale factor larger than 1.

### 3.4 Systematic uncertainties

In the results presented above, the only systematic uncertainty that has been considered is 10 per cent in the *Fermi*-LAT best-fitting flux normalization (see Appendix A2), resulting from the systematic uncertainty in the LAT collection area. This is added in quadrature to its statistical uncertainty, and therefore contributes to the statistical uncertainties in the EBL parameters reported in Table 3. In the rest of this section, we discuss systematic uncertainties in the MAGIC results, and how they affect the EBL estimation.

As mentioned above, the EBL estimation method adopted here relies on the assumption that the chosen spectral models are a good representation of the intrinsic gamma-ray spectra of the blazars in the data set. The derived best-fitting EBL density and its statistical uncertainty range are correct only as long as this assumption holds. This is one of the main sources of systematic uncertainty of this method. In order to estimate its effect in our results, we have performed the following tests:

(i) Include the power law into the pool of eligible functions.
(ii) Perform the model selection at a fixed, low level of EBL density.

When the power law is added to the pool of eligible functions in the process described in Section 3.2, it is preferred to all the others (i.e. yields the highest fit $p$-value) for some of the spectra. This is the case for between 10 and 15 of the 32 spectra (depending on the EBL template) if only MAGIC data are considered. For the MAGIC and *Fermi*-LAT analysis, the number drops to between 5 and 8. For those spectra, the additional parameters in the more complex functions do not improve the fit $\chi^2$ enough to compensate for the decrease in the number of degrees of freedom, and so the power law provides the largest fit $p$-value. Choosing a power law as intrinsic spectral shape has the disadvantage that all the curvature of the *observed* spectrum will have to be explained by the EBL, even if part of the curvature is actually intrinsic. This will bias the best-fitting EBL scale towards larger values, since the effect will likely go in the same direction for all sources (intrinsic VHE spectra are expected to become generally softer with energy). For this reason we excluded the power law for the EBL estimates reported in Table 3, and we only perform the test (i) in order to estimate the high end of the systematic uncertainty related to the choice of spectral model.

In a second test (ii) we re-evaluate the model selection (again based on $p$-values), but fixing the EBL density (for the EBL template being used) at a level determined, at $\lambda = 1.1$ μm, by the galaxy counts measurement in Madau & Pozzetti (2000): specifically, we use the best-fitting value minus $1\,\sigma$, i.e. $7.81\,\mathrm{nW\,m^{-2}\,sr^{-1}}$ (this measurement is shown later in Fig. 11). By forcing a low EBL density (instead of scanning a wide range) during model selection, we naturally favour more complex functions that can account for part of the observed spectral curvature. The total number of free intrinsic spectral parameters is hence slightly larger, between 2 and 6 more parameters for a total of $\simeq$105 parameters ($\simeq$115 for the *Fermi* + MAGIC analysis), depending on the EBL template. The EBL density estimation with this new set of spectral models will then result in weaker constraints (larger uncertainties) on the low end, due to the larger degeneracy between intrinsic spectra and the effect of the EBL.

The other main source of systematic uncertainties we consider, which is related to the IACT observation technique, is the systematic uncertainty in the absolute 'energy scale' of the MAGIC telescopes – or, to be more precise, in the total light throughput of the atmosphere and the telescopes. The reconstruction of the energy of gamma-rays detected by IACTs fully relies on MC simulations of the



Downloaded from https://academic.oup.com/mnras/article-abstract/486/3/4233/5427920 by Universita degli Studi di Pisa user on 10 April 2020

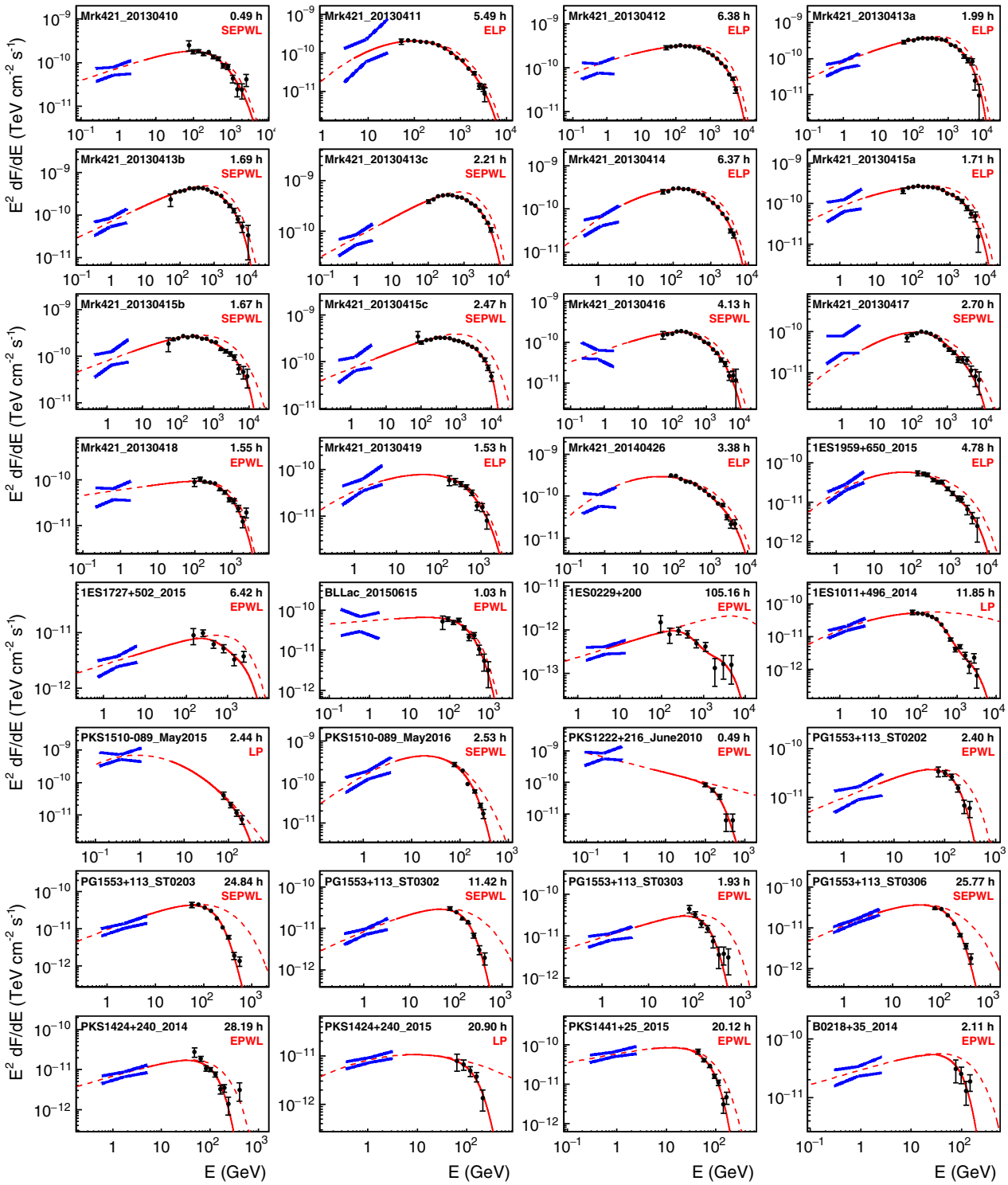


**Figure 5.** Spectral energy distributions of the 32 spectra measured by MAGIC (black points) and *Fermi*-LAT (blue bow-ties). The fits correspond to the analysis that uses the D11 EBL template and a single free EBL parameter (overall scale factor) – see Table 3. The dashed red curves are the best-fitting intrinsic spectra, the functional form of which is shown in red (as an acronym) below the observation time. The solid curves are the corresponding absorbed spectra. Each of the individual spectral points (black dots) is obtained from the excess of gamma-like events in a given bin of *estimated* energy $E_{\rm est}$; the corresponding flux is evaluated at the median *true* energy of the events (as estimated from the MC simulation).

Downloaded from https://academic.oup.com/mnras/article-abstract/486/3/4233/5427920 by Universita degli Studi di Pisa user on 10 April 2020

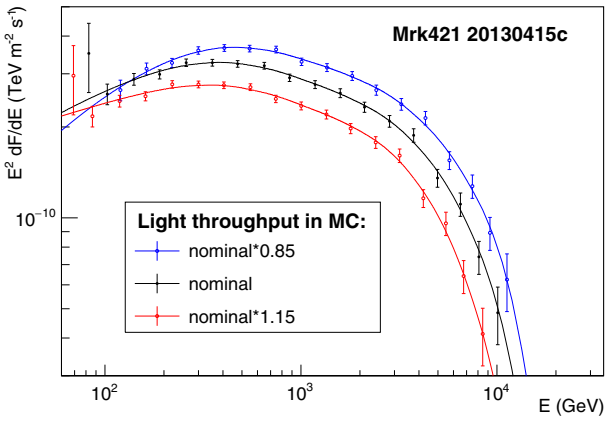


**Figure 6.** Observed SED of one of the Mrk 421 samples analysed with three different assumptions on the total overall light throughput of the atmosphere and the telescopes.

shower development in the atmosphere and of the light detection by the telescopes. Any mismatch between the MC-simulated and the actual values of, for instance, the transparency of the atmosphere, or the light collection efficiency of the telescopes, will result in a systematic error in the estimated energy. The MC model is tuned to the characteristics of the telescopes during periods of stable performance (typically lasting several months), and for typical good observation conditions. It is however not tuned to the conditions of each observation night, therefore variations of atmospheric transparency or telescope efficiency *within a period* contribute to the *statistical* uncertainties reported in the previous section. In order to estimate the effect on the EBL uncertainty of the possible *average* data-MC mismatch, we adopt the estimate in Aleksić et al. (2016b) of a maximum ±15 per cent departure in the absolute energy scale, and

(iii) re-analyse the whole data set using spectra reconstructed with MAGIC IRFs corresponding to a total light throughput between 85 per cent and 115 per cent of the nominal one, in steps of 5 per cent (i.e. six different assumptions, besides the case of nominal efficiency).

An example of the effect of those modifications of the IRFs on one of the spectra of the sample is shown on Fig. 6.

The whole EBL estimation procedure, including spectral shape selection, was repeated independently for each of these six assumptions on the average MC-data mismatch in light throughput. The envelope of the $1\sigma_{\rm stat}$ statistical uncertainty ranges of the nine different analyses (the default one, the two with modified spectral model selection, and the six with modified light throughput) is taken as the total uncertainty, including systematic uncertainties, reported in Table 4. The total uncertainties are around twice as large (or larger) as statistical uncertainties, showing that this EBL determination method, applied to our data sample, is limited by systematic uncertainties. The lower end of the systematic uncertainty is set, practically in all cases, by the test (ii) described above, hence linked to spectral model selection – the only exception is the I13 template (which is an outlier in terms of EBL spectral shape), for which it is set by the scan of light throughputs (iii). For the upper end of the systematic uncertainty, in contrast, there is no clear pattern: it is sometimes determined by the changes in light throughput (iii), and in other cases by the inclusion of the power law as an allowed intrinsic spectral model (i).

**Table 4.** EBL density constraints using MAGIC and MAGIC + *Fermi*-LAT spectra, including systematic uncertainties.

| EBL template | MAGIC-only (stat + sys) | MAGIC + *Fermi*-LAT (stat + sys) |
|---|---|---|
| D11 | 0.92 (+0.23, −0.18) | 1.00 (+0.10, −0.18) |
| Fi10 | 0.96 (+0.17, −0.28) | 1.00 (+0.09, −0.18) |
| F08 | 0.99 (+0.21, −0.23) | 1.04 (+0.10, −0.20) |
| G12 | 0.97 (+0.26, −0.22) | 1.03 (+0.10, −0.20) |
| H12 | 1.24 (+0.21, −0.41) | 1.21 (+0.19, −0.15) |
| I13 | 0.82 (+0.50, −0.21) | 1.04 (+0.58, −0.34) |
| S16 | 1.33 (+0.34, −0.40) | 1.38 (+0.28, −0.34) |
| K10 | 1.23 (+0.33, −0.30) | 1.31 (+0.27, −0.23) |

A possible additional source of systematic errors is the lack of *strict* simultaneity of the MAGIC and *Fermi*-LAT observations (see Section 2.2), since source variability may lead to the average emission state being different for the two data sets. Given the stochastic nature of the behaviour of blazars, however, the systematic errors induced by this mismatch in each of the analysed spectra will likely affect the EBL estimation in different directions, rather than consistently under- or overestimate it. This will in turn result in a flattening of the minima of the profile likelihood curves, and an increase of the statistical uncertainties (relative to the ones we would obtain for truly simultaneous MAGIC and *Fermi*-LAT observations). Beyond that, we currently have no way of estimating the contribution of this effect to the final systematic uncertainty of our measurement.

### 3.5 Constraints in bins of redshift

Recent measurements of the SFH are consistent with a strong peak in the star formation rate around $z \sim 2$, decreasing gradually by about one order of magnitude towards $z = 0$ as shown by Madau & Dickinson (2014). Since the EBL is a tracer of the SFH, any bias in how star formation rate and galaxy evolution are treated in the EBL models could potentially have an effect in our constraints. While the ideal instrument to test the imprint of SFR evolution on gamma-ray blazar spectra is *Fermi*-LAT, as it can detect sources up to larger distances, the samples presented in this work at $z \gtrsim 0.5$ are also good candidates to test whether there is any departure in the measured optical depth with respect to the EBL model predictions.

In order to probe the evolution of the EBL, the data were divided in four redshift bins (0.0–0.1, 0.1–0.3, 0.3–0.6, and 0.6–1.0, see Table 1) and individual $\alpha_i$ optical depth scaling factors were derived for each bin. The intrinsic spectral models for each of the spectra are the same as in the global EBL scale determination using all redshift bins together (but of course the likelihood maximization is re-done in each bin separately, hence the best-fitting spectral parameters are in general different). For the D11 template, the results are presented in Fig. 7. As expected, the strongest constraints are obtained for the two lowest redshift bins, dominated by the high-quality spectra of Mrk 421 and 1ES 1011+496, respectively. The 3rd and 4th bins mostly reflect contributions from PG 1553+113 (strong upper bounds), PKS 1424+240 and PKS 1441 + 25. Only the 3rd bin, $0.3 < z < 0.6$, shows $> 1\sigma_{\rm stat}$ deviations from $\alpha = 1$ (both for the MAGIC and for the MAGIC + *Fermi*-LAT analyses). For that redshift range, as well as for $0.6 < z < 1.0$, the effect of EBL attenuation and the intrinsic spectral curvature are hard to disentangle, and the corresponding parameters are degenerate. As a consequence, the expected EBL imprint can be well reproduced with an exponential or superexponential cut-off, and hence the best-



Downloaded from https://academic.oup.com/mnras/article-abstract/486/3/4233/5427920 by Universita degli Studi di Pisa user on 10 April 2020

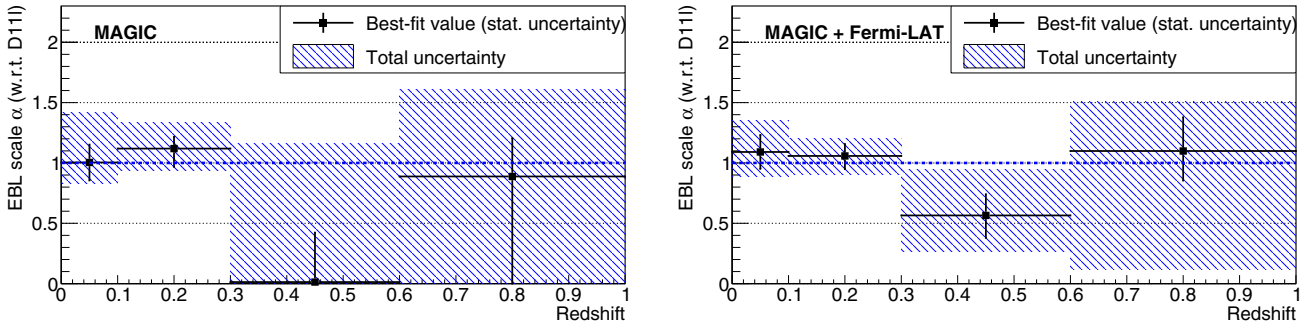


**Figure 7.** EBL scale, relative to the D11 model, in four bins of redshift. Left-hand panel: MAGIC-only analysis; right-hand panel: MAGIC + Fermi-LAT analysis. The dashed blue band shows the total uncertainty including systematics.

fitting $\alpha$, especially for the MAGIC-only analysis, can be well below 1 (even at 0, see left-hand panel of Fig. 7). The same effect is visible on the PG 1553 curves in Fig. 4. Nevertheless, the results in all redshift bins are compatible (at the $\simeq 1\sigma$ level) with the EBL density in the D11 model, once systematic uncertainties are taken into account. It must be noted that the *Fermi*-LAT + MAGIC result in the highest redshift bin, when only statistical uncertainties are considered, represents the first detection of the imprint of the EBL using IACT observations of $z > 0.6$ blazars.

### 3.6 Fit residuals

Many extensions of the Standard Model of particle physics, particularly those linked to superstring theories, suggest the existence of light zero-spin bosons commonly known as axion-like particles (ALPs). In the presence of magnetic fields (which exist not only in galaxies, but also on larger scales in the intergalactic space), photon-ALP oscillations are expected to occur if these bosons exist (see e.g. de Angelis, Roncadelli & Mansutti 2007; Hooper & Serpico 2007; Mirizzi, Raffelt & Serpico 2007; Sánchez-Conde et al. 2009; de Angelis, Galanti & Roncadelli 2011). ALPs travel unaffected by interactions with EBL photons, and can oscillate back into VHE photons close to us. This can potentially lead to significant modifications of the effective optical depth $\tau$ that we measure from Earth, modifying the observed source spectra in non-trivial ways, or even making the Universe significantly more transparent to gamma-rays at certain energies.

Several studies by de Angelis et al. (2009), Domínguez, Sánchez-Conde & Prada (2011a), Tavecchio et al. (2012), and Meyer, Horns & Raue (2013) have reported hints of such coupling between gamma-ray photons coming from blazars and the hypothetical bosons over the past years. They are all based on observations of an apparent hardening or 'pile-up' in the estimated intrinsic VHE spectra of several blazars, once observations are corrected for the effect of the EBL according to a given model. Other authors have found no evidence of this sort of anomaly (e.g. Sanchez, Fegan & Giebels 2013; Biteau & Williams 2015; Domínguez & Ajello 2015)
.

In order to test the agreement between our results and previous studies suggesting the existence of such oscillations, we present, in Fig. 8, the fit residuals (in standard deviations) as a function of the EBL optical depth (as predicted by the D11 template). Each of the points corresponds to one bin of estimated energy in one of the 32 VHE spectra of the analysed sample. In the analysis, all the bins containing at least one on- or off-source event are used, regardless of whether or not there was a significant excess of gamma-like events

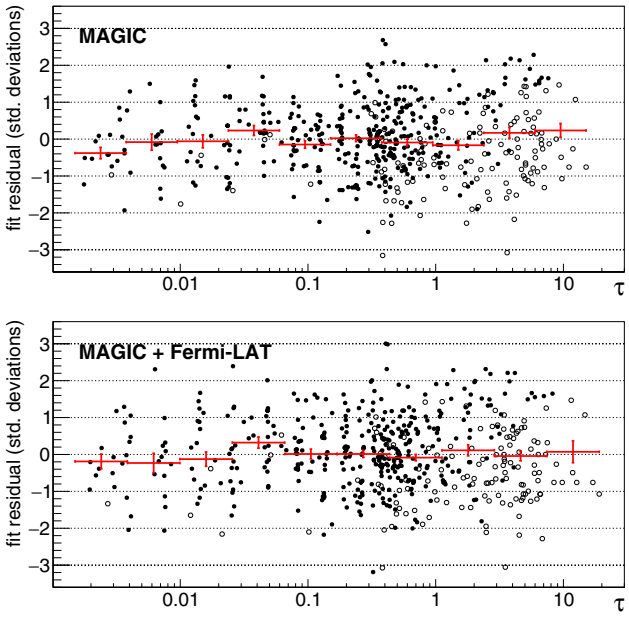


**Figure 8.** Fit residuals versus optical depth $\tau$, for the MAGIC data points (i.e. bins of estimated energy). Top panel: MAGIC-only analysis. Bottom panel: MAGIC + *Fermi*-LAT analysis. Filled symbols indicate bins in which there is a $> 1.5\,\sigma$ excess of gamma-like events above the background fluctuations. The optical depth is calculated for the best-fitting EBL scale, relative to the D11 template. The red graph is the average residual in 10 bins of $\tau$.

from the source in the bin.[4] This approach avoids the possible bias resulting, in the low-statistics regime, from keeping upward-fluctuating spectral points while rejecting those under the noise level. The estimated energy bins in which there is a gamma-ray excess larger than $1.5\sigma$ are shown in Fig. 8 as filled symbols, and display the expected bias towards positive values, particularly at high optical depths. When all bins in the analysis are considered, fit residuals show, at all optical depths, the expected behaviour in absence of anomalies, fluctuating around 0. We have defined 10 bins in $\tau$, and computed the average residuals in them. The results, both for the analysis that uses only MAGIC data and the

[4]The VHE SEDs obtained with MAGIC that are shown throughout the paper only show points with significant gamma-ray excesses (relative statistical uncertainty of the flux smaller than 50 per cent) – but the number of energy bins used in the analysis is much larger.

Downloaded from https://academic.oup.com/mnras/article-abstract/486/3/4233/5427920 by Universita degli Studi di Pisa user on 10 April 2020

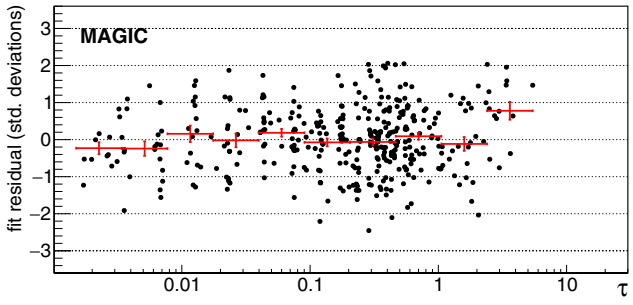


**Figure 9.** Fit residuals versus optical depth $\tau$, for the MAGIC-only analysis performed after removing low significance points ($<1.5\sigma$, see the text).

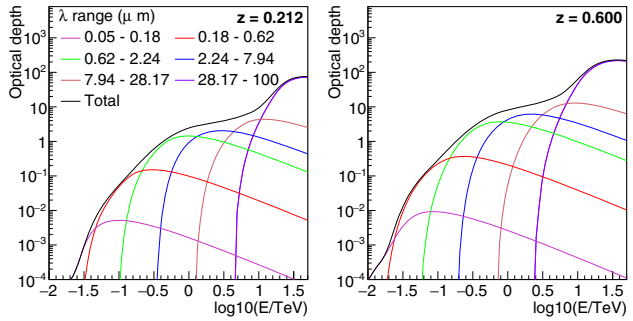


**Figure 10.** Optical depth due to the EBL in five different ranges of wavelength (units: microns), for the D11 model and two different redshifts. The optical depth in each of the five ranges is scaled by an independent free parameter during the likelihood maximization.

one using MAGIC + *Fermi*-LAT, show that the observed attenuation is compatible with the optical depth predictions from the D11 EBL model. When the analysis is repeated using for each spectrum only the range of estimated energy within which all bins have a $\geq 1.5\sigma$ gamma-like excess (Fig. 9), the residual for the highest optical depth bin becomes significantly biased towards positive values. In our case the effect is modest ($\simeq 3\sigma$), but we think it may be partly responsible for the above-mentioned claims of anomalous transparency found in the literature. For this reason, we have also included bins without significant gamma-ray excesses in the computation of the likelihood from which we derive our EBL constraints.

## 4 WAVELENGTH-RESOLVED EBL DETERMINATION

Throughout Section 3 we have assumed that both the evolution and the shape of the spectrum of the EBL were exactly those of the template EBL model adopted in each case, i.e. the energy- and redshift-dependence of the total optical depth were fixed, with a single overall scaling factor as free EBL parameter. For three of the templates (D11, Fi10, G12) we have available, besides the total optical depth $\tau(E, z)$, the optical depths due to the EBL in six independent wavelength ranges, limited by the values $\lambda = 0.05$, 0.18, 0.62, 2.24, 7.94, 28.17, and 100 μm (see Fig. 10), where the values of $\lambda$ correspond to the EBL wavelengths at $z = 0$.

### 4.1 Methodology

By scaling each of these six $\tau_i(E, z)$ with an independent factor $\alpha_i$, one can obtain the total optical depth as $\tau(E, z) = \sum_i \alpha_i \tau_i(E, z)$. The six values $\alpha_i$ can then be treated as independent free parameters in the likelihood maximization (see Section 3.1), providing a handle on the shape of the EBL spectrum. Note that we do not introduce any correlation between the six parameters to impose a 'smooth' EBL spectrum. The total optical depth for a given $z$, however, will behave quite smoothly versus $E$ because each of the $\tau_i(E)$ curves has significant overlap with the ones of the neighbouring EBL wavelength bins. The evolution of the EBL – which determines the redshift dependence of the $\tau_i$ values – is still fixed to the one of the given EBL model. Finally, the $1\,\sigma$ statistical uncertainties for the best-fitting values of each $\alpha_i$ are obtained using MINOS (Brun & Rademakers 1997; Hatlo et al. 2005), considering the rest of the EBL parameters $\alpha_j$, with $j \neq i$, as nuisance.

The measurement of the near-UV portion of the EBL spectrum is a powerful proxy to study the SFH of the Universe and has important cosmological implications. In addition, this is one of the bands where EBL models diverge the most (see top panel of Fig. 3), and is directly accessible through observations of GRBs at high redshifts with *Fermi*-LAT, as described by Desai et al. (2017). It has to be noted that for MAGIC the optical depth $\tau_1$ due to the EBL in the first of the wavelength bins (0.05−0.18 μm) is, according to the considered models, smaller than $10^{-2}$ for all energies and redshifts in our data sample (see Fig. 10). Therefore, its influence on the likelihood is negligible, and we cannot effectively constrain the corresponding scaling factor $\alpha_1$ (unless it was considerably larger than 1, well above the models). Besides, on Fig. 10 it can be seen that the contribution of $\tau_1$ to the total $\tau$ is rather degenerate with that of $\tau_2$, which results in problematic $-2\log L$ minima if $\alpha_1$ is allowed to take arbitrarily large values. To address this issue, we have simply constrained $\alpha_1$ to be less than 5, meaning that the EBL density in that wavelength range is less than 5 times the EBL model estimate. The results of the fit for $\alpha_1$ typically cover the whole allowed range 0–5 at the $1\sigma_{\rm stat}$ level, and are therefore not reported since they provide no useful information.

The additional freedom in the EBL modelling (relative to the simple fitting of the overall EBL density) naturally increases the degeneracy between the intrinsic spectral parameters and the EBL parameters. Consequently, the wavelength-dependent EBL determination is only possible using the MAGIC data together with the *Fermi*-LAT constraints: without the latter, the method fails to converge in most of the cases on a valid minimum of the $-2\log L$ function, due to the large degeneracy between the EBL and the spectral curvature. It is important to note that this cannot be overcome by simply reducing the number of parameters of intrinsic spectral models, since it would result in the EBL model 'absorbing' intrinsic features of the source spectra. For each spectrum, the same intrinsic spectral *model* that was chosen in the determination of the EBL density was used. The fit is however started from scratch – neither the intrinsic spectral parameters nor the EBL scaling factors from the previous single-parameter EBL density determination are known to the multi-EBL-parameter fitting algorithm. With this procedure we can test whether our blazar data *prefer* an EBL spectral shape different from the one in D11, Fi10, and G12, through an LRT in which the two competing models differ in the number of free EBL parameters.

### 4.2 Results

Using the procedure described above, we fit the data using individual optical depth scaling factors for each EBL wavelength bin. We perform the analysis independently for the three EBL templates for which we have wavelength-resolved optical depths, i.e. D11, Fi10, and G12. In each case, best-fitting scaling factors, statistical



Downloaded from https://academic.oup.com/mnras/article-abstract/486/3/4233/5427920 by Universita degli Studi di Pisa user on 10 April 2020

uncertainties, and $p$-values are obtained and reported in Table 5, and the resulting EBL SED for the D11 template is shown in Fig. 11. As a reference, the figure also shows direct measurements (open markers), galaxy counts measurements (filled markers, to be interpreted as lower limits) and the SED of the EBL from the template of D11. The results in all bands but the one in the range of 0.18–0.62 μm are compatible with the template of D11 within $1\sigma_{\rm stat}$. Note that in the calculation of the uncertainties of a given $\alpha_i$, all the other $\alpha_j$ ($j \neq i$) are treated as nuisance parameters. For the D11 case, the fit has a total of 121 free parameters (including the six $\alpha_i$ factors). The number of data points is 585 (521 energy bins of MAGIC spectra + 32 *Fermi*-LAT fluxes + 32 *Fermi*-LAT photon indices, see Appendix A2), hence resulting in 464 degrees of freedom. Since the intrinsic spectral models are the same as in the single-parameter EBL density determination, this fit has five additional free parameters. Comparing the final $L_{\rm max}$ values in both cases, we have $\Delta(-2\log(L_{\rm max})) = \Delta\chi^2 = 12.37$. This means, for $\Delta n_{\rm d.o.f.} = 5$, that our wavelength-resolved best-fitting model is only marginally favoured by the data with respect to the globally scaled D11 model in Table 3, at the $2.1\sigma$ level.[5] The situation is similar for the Fi10 model (wavelength-resolved best-fitting model preferred at the $2.4\sigma$ level), whereas for the G12 model the preference for a modified EBL spectral shape relative to the one in the model is even weaker ($1.2\sigma$).

### 4.3 Systematic uncertainties

Systematic uncertainties are evaluated with the same approach described in Section 3.4. The systematic uncertainty band shown in Fig. 11 for each wavelength bin is the envelope of the $1\sigma_{\rm stat}$ bands for all the analyses performed (with different intrinsic spectral models selection and different IRFs). Note that the effect of systematic uncertainties is most relevant at the low end of the uncertainty band – which reaches 0 (no EBL) for the two wavelength bins above 7.94 μm. Even when only the systematics associated with the choice of intrinsic spectral models are considered, the result is basically the same – meaning that, for this data set, reducing the *assumed* systematic uncertainty on the average absolute calibration of the telescopes would not improve the result significantly. On the other hand, a hypothetical reduction of the actual systematic *error* via for example run-wise correction of the data, could well result in a reduction of the statistical uncertainties of the measurement. The main limitation of this technique is currently that the effect of the EBL on the VHE spectra is, for most of the explored wavelength range, hardly discernible from plausible intrinsic spectral features like cut-offs. Only in the 0.62–2.24 μm range is the lower end of the systematic uncertainty band clearly above 0, because the constraint in this range is dominated by the inflection point in the $\tau$ versus $log(E)$ curves at around 1 TeV, a feature that in our sample is most visible in the SED of 1ES 1011+496 (see Fig. 5 and Ahnen et al. 2016a). Since such a feature cannot be fitted by any of the considered intrinsic spectral models (all of which are concave functions, with no inflection points), a reduction of the EBL density from its best-fitting value results in a fast worsening of the fit quality, hence providing a meaningful lower bound. On the other hand, the high end of the uncertainty bands is determined mainly by the fact that for too high EBL density, the intrinsic spectra would have to become convex (which is forbidden by construction) to reproduce the MAGIC observations. These upper constraints are only slightly increased when systematic uncertainties are taken into account.

We also obtained wavelength-resolved EBL measurements like those shown in Fig. 11 using the G12 and Fi10 EBL models. This allowed us to estimate the contribution of the choice of the EBL template (spectrum and evolution) to the total systematic uncertainty. The envelope of the total uncertainty bands of the three analyses (D11, G12, Fi10) is shown as the hashed area in Fig. 12, where the results are compared to five EBL models (including those used in the calculations), and again on Fig. 13, which displays also other measurements based on gamma-ray observations. The corresponding $\lambda F_\lambda$ values and uncertainties at the centre of the wavelength bins are reported on Table 6 for the wavelength-resolved analyses carried out with the D11, Fi10, and G12 templates.

### 4.4 Discussion

The most constraining results we obtain correspond to the two bins in the range 0.62–7.94 μm, for which the statistical uncertainties in the EBL density are around 10 per cent. When systematic uncertainties are considered, only the range 0.62–2.24 μm provides a meaningful lower bound on the EBL density, which is at the level of the galaxy counts measurements reported in Madau & Pozzetti (2000) (the filled red points in Fig. 11). The best-fitting values and the upper end of the total uncertainty band are, respectively, ≃30 per cent and ≃75 per cent above those measurements, meaning that most of the EBL in that wavelength range (red and near-infrared) is already resolved in individual galaxies. The result is 17 per cent ($1.9\sigma_{\rm stat}$) above the D11 model (which models the total EBL, including the contribution from unresolved sources of known classes), but compatible with it within systematics. In the few μm range, our results are clearly inconsistent with the direct measurements reported in Matsumoto et al. (2015), indicating that the large excess of isotropic near-infrared emission claimed in that work is not of extragalactic origin. At wavelengths above 7.94 μm, where direct measurements are scarce, and EBL models differ significantly, our results are compatible with all the considered models at the $\simeq 1\sigma_{\rm stat}$ level, and even with zero (no EBL) within systematics.

For the shortest wavelength bin considered in this study, 0.05–0.18 μm (*not* displayed in Figs 11–13), the optical depths from the interaction of VHE gamma-rays with such short-wavelength EBL photons are simply too low for the range of redshifts (and gamma-ray energies) covered by our sample. In the 0.18–0.62 μm range our result is $2.8\sigma_{\rm stat}$ above the EBL density in the D11 model (2.7 and $1.7\sigma_{\rm stat}$, respectively, for Fi10 and G12), see Table 5 and Fig. 11. This hint of higher-than-expected EBL in the UV-visible may well be just the result of systematic uncertainties – note that the EBL density from all three models is within the estimated systematic uncertainty band. But it is interesting to note that our result matches the direct measurement from Mattila et al. (2017) using the 'dark cloud' method (Fig. 11). In contrast, the estimate reported by Abdollahi et al. (2018) in the range 0.09–4.5 μm, based on *Fermi*-LAT observations of a sample of 739 blazars up to redshift $z \simeq 3.0$, is in good agreement with the D11 model.

The short-wavelength EBL excess in our analysis is strongly reduced if the five PG 1553+113 spectra are excluded from the sample. In such case, the best-fitting scale factor becomes $\alpha_{0.18-0.62\,\mu\rm m} = 1.6 \pm 0.9_{\rm stat}$, which is compatible with 1. Indeed, PG 1553+113, given its redshift of $z \geq 0.43$ and the good quality of the obtained spectra, dominates the measurement at these EBL wavelengths. Its effect on the result may seem at odds with

[5] $2.4\sigma$ for $\Delta n_{\rm dof} = 4$, if we consider that $\alpha_1$ is constrained to be between 0 and 5, and hence not a completely free parameter.

Downloaded from https://academic.oup.com/mnras/article-abstract/486/3/4233/5427920 by Universita degli Studi di Pisa user on 10 April 2020

**Table 5.** Wavelength-resolved EBL constraints (scaling factors relative to three models) using MAGIC + *Fermi*-LAT spectra.

| | EBL wavelength range (μm, @ $z = 0$) | | | | | $p$-value |
|---|---|---|---|---|---|---|
| EBL model | 0.18–0.62 | 0.62–2.24 | 2.24–7.94 | 7.94–28.17 | 28.17–100 | |
| D11 (stat): | 2.60 (+0.56, −0.57) | 1.17 (+0.09, −0.10) | 1.10 (+0.12, −0.13) | 1.13 (+0.25, −0.24) | 1.62 (+0.99, −0.77) | $1.15 \times 10^{-3}$ |
| (stat + sys): | (+0.93, −1.72) | (+0.19, −0.27) | (+0.15, −0.69) | (+0.25, −1.13) | (+1.31, −1.62) | |
| Fi10 (stat): | 1.89 (+0.58, −0.33) | 1.04 (+0.12, −0.06) | 1.05 (+0.11, −0.10) | 0.68 (+0.18, −0.16) | 2.40 (+1.65, −1.32) | $0.91 \times 10^{-3}$ |
| (stat + sys): | (+0.77, −1.10) | (+0.25, −0.23) | (+0.17, −0.59) | (+0.37, −0.68) | (+4.24, −2.40) | |
| G12 (stat): | 1.45 (+0.35, −0.26) | 1.01 (+0.10, −0.07) | 1.03 (+0.10, −0.10) | 1.16 (+0.27, −0.25) | 2.01 (+1.13, −0.89) | $1.53 \times 10^{-3}$ |
| (stat + sys): | (+0.82, −0.97) | (+0.25, −0.22) | (+0.16, −0.63) | (+0.30, −1.16) | (+1.13, −2.01) | |

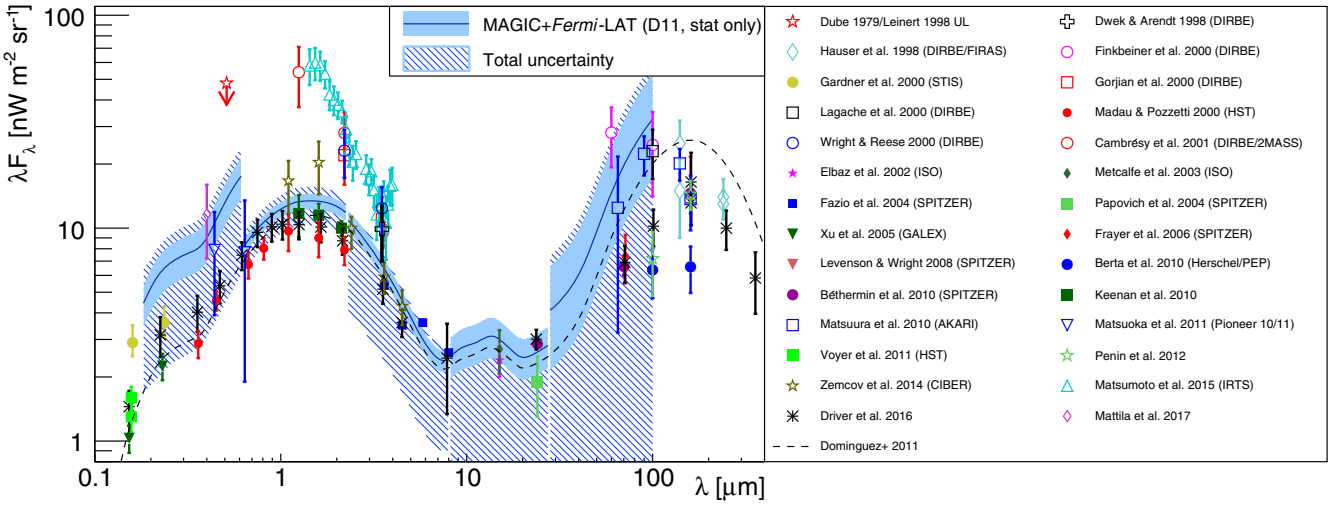


**Figure 11.** Wavelength-resolved EBL measurement using MAGIC and *Fermi*-LAT observations, relative to the D11 EBL model at $z = 0$, in five wavelength bins. A collection of direct EBL measurements is shown for comparison, taken from Berta et al. (2010), Béthermin et al. (2010), Cambrésy et al. (2001), Driver et al. (2016), Dube, Wickes & Wilkinson (1979), Leinert et al. (1998), Dwek & Arendt (1998), Elbaz et al. (2002), Fazio et al. (2004), Finkbeiner, Davis & Schlegel (2000), Frayer et al. (2006), Gardner et al. (2000), Gorjian et al. (2000), Hauser et al. (1998), Keenan et al. (2010), Lagache et al. (2000), Levenson & Wright (2008), Madau & Pozzetti (2000), Mattila et al. (2017), Matsumoto et al. (2015), Matsuoka et al. (2011), Matsuura et al. (2011), Metcalfe et al. (2003), Papovich et al. (2004), Pénin et al. (2012), Voyer et al. (2011), Wright & Reese (2000), Xu et al. (2005), and Zemcov et al. (2014). Filled symbols correspond to galaxy counts and should therefore be interpreted as lower limits.

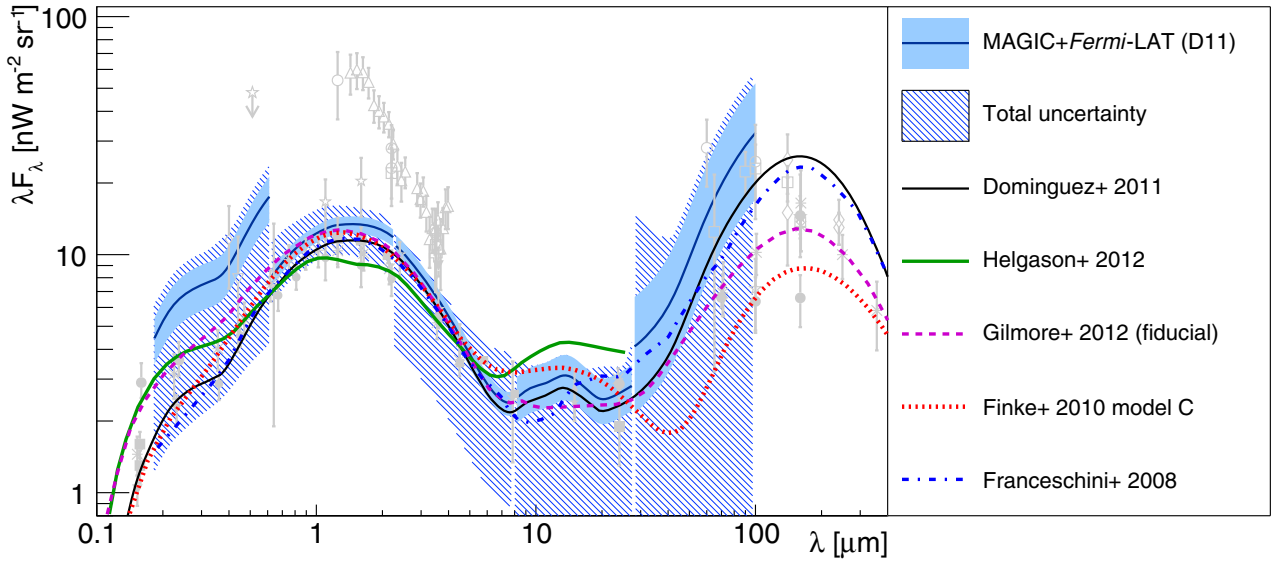


**Figure 12.** Wavelength-resolved EBL measurement using MAGIC and *Fermi*-LAT observations. The solid band, obtained with the D11 model, is the same as in Fig. 11; the systematic uncertainty band is the envelope of the bands obtained with three EBL templates (D11, Fi10, and G12). The result is compared to the EBL SED (at $z = 0$) for several models. Light grey symbols are the direct measurements shown in Fig. 11.



Downloaded from https://academic.oup.com/mnras/article-abstract/486/3/4233/5427920 by Universita degli Studi di Pisa user on 10 April 2020

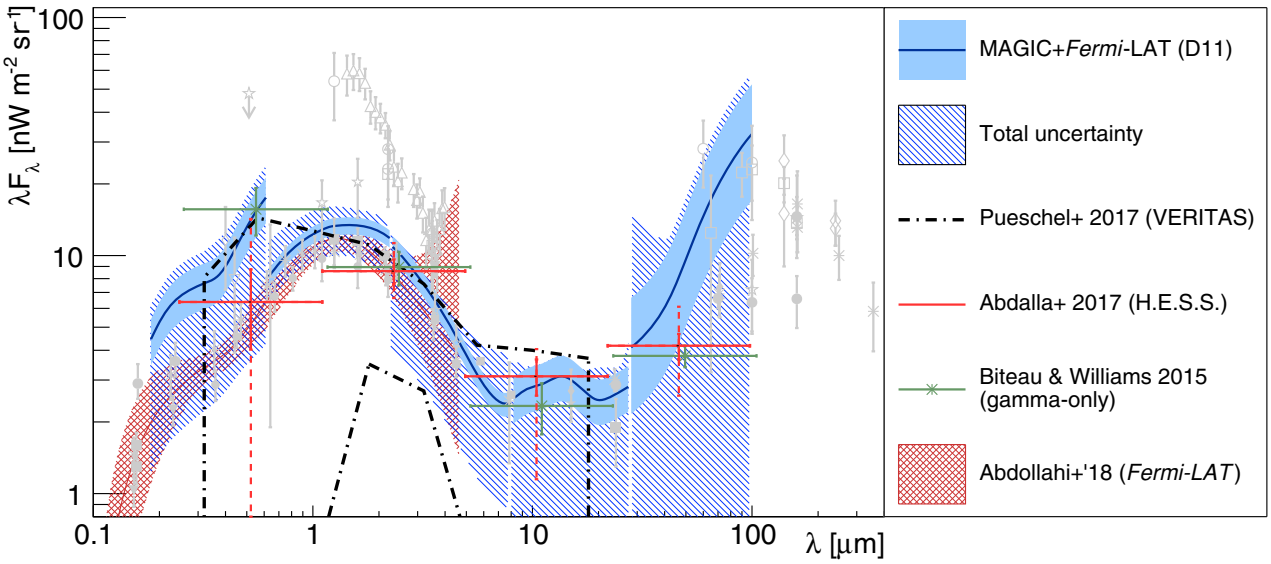


**Figure 13.** Wavelength-resolved EBL measurement using MAGIC and *Fermi*-LAT observations (same as in Fig. 12) compared to other EBL measurements obtained with gamma-ray observations, taken from Pueschel (2017), Abdalla et al. (2017), Biteau & Williams (2015), and Abdollahi et al. (2018).

**Table 6.** Wavelength-resolved $\lambda F_\lambda$ EBL constraints from MAGIC + *Fermi*-LAT spectra for three models, D11, Fi10, G12, evaluated at the centre of the λ ranges in Table 5. For each model, the first column shows the best-fitting value, the other two are the statistical and total uncertainties, respectively. Units are (nW m$^{-2}$ sr$^{-1}$).

| λ (μm) | | D11 | | | Fi10 | | | G12 | |
|---|---|---|---|---|---|---|---|---|---|
| 0.33 | 7.8 | $^{+1.6}_{-1.7}$ | $^{+2.8}_{-5.1}$ | 6.6 | $^{+2.0}_{-1.1}$ | $^{+2.7}_{-3.8}$ | 6.9 | $^{+1.7}_{-1.2}$ | $^{+3.9}_{-4.6}$ |
| 1.18 | 13.2 | $^{+1.0}_{-1.1}$ | $^{+2.1}_{-3.1}$ | 12.8 | $^{+1.4}_{-0.7}$ | $^{+3.1}_{-2.8}$ | 12.8 | $^{+1.3}_{-0.9}$ | $^{+3.2}_{-2.7}$ |
| 4.22 | 5.1 | $^{+0.6}_{-0.6}$ | $^{+0.7}_{-3.2}$ | 5.1 | $^{+0.6}_{-0.5}$ | $^{+0.8}_{-2.9}$ | 4.9 | $^{+0.5}_{-0.5}$ | $^{+0.8}_{-3.0}$ |
| 15.0 | 3.0 | $^{+0.7}_{-0.6}$ | $^{+0.7}_{-3.0}$ | 2.2 | $^{+0.6}_{-0.5}$ | $^{+1.2}_{-2.2}$ | 2.7 | $^{+0.6}_{-0.6}$ | $^{+0.7}_{-2.8}$ |
| 53.1 | 11.1 | $^{+6.8}_{-5.3}$ | $^{+9.0}_{-11.1}$ | 5.4 | $^{+3.7}_{-3.0}$ | $^{+9.5}_{-5.4}$ | 10.3 | $^{+5.8}_{-4.6}$ | $^{+5.8}_{-10.3}$ |

the outcome of the MAGIC + *Fermi*-LAT single-EBL-parameter analysis when only the five spectra from this source are used. In that case, the best-fitting scale was well below 1 (see the corresponding profile likelihood curve in the bottom panel of Fig. 4). We must remark, however, that in the adopted method, the best-fitting EBL values are those that result in the maximum likelihood with plausible *shapes* of the intrinsic spectra. The absolute fluxes are irrelevant, as we do not measure absolute absorption factors (because the intrinsic spectra are not known). Therefore, a given observed VHE spectrum is not bound to shift the EBL results always in a given direction, but its effect depends on the other spectra included in the sample. In the case at hand, the rest of the sources constrain the EBL in the 0.62–2.24 μm to be close to the one in the models, and hence a low EBL in the $< 0.62$ μm range would probably imply an unnatural (significantly convex) intrinsic spectrum for PG 1553+113. This just shows that there is *no contradiction* in the different effect of PG 1553+113 on the two types of analysis – but provides no insight on whether the hint of an excess is genuine or not.

A comparison of our results with previous EBL constraints based on gamma-ray observations is shown in Fig. 13. Those that include an evaluation of systematic uncertainties (Abdalla et al. 2017; Pueschel 2017) show similar features to our own, with weak or no lower constraint except in the few μm range, and similar upper bounds.

## 5 SUMMARY AND CONCLUSIONS

We presented a measurement of the EBL using MAGIC and *Fermi*-LAT gamma-ray observations of 12 blazars in different periods, for a total of 32 spectra. A model of the EBL (with one or more free parameters) and a set of plausible models for the 32 intrinsic spectra are used to construct a likelihood. This likelihood is then maximized to obtain the EBL model parameters most compatible with the MAGIC and *Fermi*-LAT observations. The main results are the following:

(i) With only one free EBL parameter (global EBL density for fixed SED and evolution) it is possible to set constraints both with the MAGIC data alone, and with the combination of MAGIC and *Fermi*-LAT contemporaneous observations. The results, shown in Tables 3 and 4, are compatible at the $1\sigma_{\rm stat}$ level with the EBL density in the D11, Fi10, F08, and G12 templates. The other four tested templates (H12, I13, S16, and K10) are in worse agreement with our observations, with EBL densities up to $3.5\sigma_{\rm stat}$ off the best-fitting values. The data do not allow to discriminate clearly among the models, although the first four seem favoured by our results.

(ii) An assessment of the total uncertainties including systematics was performed by repeating the analysis in different conditions to account for the uncertain knowledge of the intrinsic spectral shapes and the absolute calibration of MAGIC. For the favoured models, the resulting upper bounds are between 13 per cent and 23 per cent above the EBL densities in the models. We conclude that our result and the described methodology are currently dominated by systematic uncertainties.

(iii) The distribution of fit residuals as a function of optical depth for the D11 template (Fig. 8) shows no hint of significant deviations. Therefore, we find no evidence of anomalies in the transparency of the Universe to gamma-rays, like those that might be attributed e.g. to photon-ALP conversions. We think that the inclusion in the analysis of bins of estimated energy for which no significant excess (or even a deficit) of gamma-like events is recorded is instrumental to avoid biases that could be misinterpreted as anomalies in the gamma-ray absorption process.

Downloaded from https://academic.oup.com/mnras/article-abstract/486/3/4233/5427920 by Universita degli Studi di Pisa user on 10 April 2020

(iv) For the D11 EBL template we repeated the analysis by dividing the sample in four bins of redshift (in the range of $z$ from 0 to 1), with the aim of probing the evolution of the EBL density relative to that in the model. The measured constraints are compatible with the model in all four bins at the $\simeq 1\sigma_{\rm stat+sys}$ level (Fig. 7). For redshifts above 0.3 the data do not allow to set any lower bound to the EBL density, once systematic uncertainties are taken into account. This is due to the degeneracy between possible intrinsic features of VHE spectra, like cut-offs, and the effect of the EBL in the range of energies accessible by MAGIC at such distances. The measured optical depth for the last redshift bin is however significantly above $\alpha = 0$ for the MAGIC + *Fermi*-LAT analysis if only statistical uncertainties are considered. It underlines the fact that, for the first time in the VHE band, we are able to effectively explore the EBL at redshift close to 1. It also sets promising prospects for future instrumentation with reduced systematic uncertainties.

(v) The combination of MAGIC and *Fermi*-LAT data allows to perform λ-resolved measurements of the EBL, for three of the models (D11, Fi10, G12), for which we have available the optical depths as a function of EBL wavelength (Tables 5 and 6 and Figs 11–13). This procedure shows that the constraints obtained with our blazar data sample are mostly driven by the EBL in the $\lambda \simeq 0.6$–8 μm range. The upper EBL bound in that range, including systematic uncertainties, is between 13 and 29 per cent higher than the models, leaving little room for additional EBL contributions not accounted for in the models. In the 0.18–0.62 μm range we obtain a relatively high EBL density, particularly with respect to the D11 and Fi10 models, but the deviation is not significant once systematic uncertainties are considered.

Finally, it must be stressed once more that the method used in this paper (and in previous similar works in the literature) for the determination of the EBL relies on the assumption that the chosen spectral blazar models can reproduce the intrinsic spectra of the blazars in the sample. We adopted a conservative approach by always allowing the intrinsic spectra to be curved (pure power laws were only tried for the estimation of systematic uncertainties). In addition, we just required a better $p$-value in order to adopt a more complex model (e.g. an LP with exponential cut-off over an LP), instead of a minimum significance of the corresponding LRT (e.g. $2\sigma$ in Biteau & Williams 2015). These differences in the methods to select intrinsic spectral models make it impossible to compare directly the merit of the different gamma-ray based EBL measurements shown in Fig. 13.

We expect that with a large sample of high-quality spectra up to the few TeV range, such as those that will be obtained in the coming years with the Cherenkov Telescope Array (CTA; Acharya et al. 2013), it will be possible to relax the assumption on the intrinsic spectral shapes, to include more general concave functions beyond those used in this work. CTA will also benefit from a better control of the systematics related with the atmospheric conditions and the absolute calibration of the telescopes. Together with the increased redshift range provided by its lower energy threshold relative to current IACTs, CTA will certainly be a major contributor to the study of the EBL.

## ACKNOWLEDGEMENTS

We would like to thank the Instituto de Astrofísica de Canarias for the excellent working conditions at the Observatorio del Roque de los Muchachos in La Palma. The financial support of the German BMBF and MPG, the Italian INFN and INAF, the Swiss National Fund SNF, the ERDF under the Spanish MINECO (FPA2015-69818-P, FPA2012-36668, FPA2015-68378-P, FPA2015-69210-C6-2-R, FPA2015-69210-C6-4-R, FPA2015-69210-C6-6-R, AYA2015-71042-P, AYA2016-76012-C3-1-P, ESP2015-71662-C2-2-P, FPA2017-90566-REDC), the Indian Department of Atomic Energy, the Japanese JSPS and MEXT and the Bulgarian Ministry of Education and Science, National RI Roadmap Project DO1-153/28.08.2018 is gratefully acknowledged. This work was also supported by the Spanish Centro de Excelencia 'Severo Ochoa' SEV-2016-0588 and SEV-2015-0548, and Unidad de Excelencia 'María de Maeztu' MDM-2014-0369, by the Croatian Science Foundation (HrZZ) Project IP-2016-06-9782 and the University of Rijeka Project 13.12.1.3.02, by the DFG Collaborative Research Centres SFB823/C4 and SFB876/C3, the Polish National Research Centre grant UMO-2016/22/M/ST9/00382 and by the Brazilian MCTIC, CNPq, and FAPERJ. The work of the author M. Nievas Rosillo is financed with grant FPU13/00618 of MECD. A. Domínguez thanks the support of the Ramón y Cajal program from the Spanish MINECO. The work of the author M. Vázquez Acosta is financed with grant RYC-2013-14660 of MINECO.

## REFERENCES

Abdalla H. et al., 2017, A&A, 606, A59
Abdo A. A. et al., 2010, ApJ, 723, 1082
Abdollahi S. et al., 2018, Science, 362, 1031
Abramowski A. et al., 2013, A&A, 550, A4
Acero F. et al., 2015, ApJS, 218, 23
Acharya B. S. et al., 2013, Astropart. Phys., 43, 3
Ackermann M. et al., 2012, Science, 338, 1190
Aharonian F. et al., 2006, Nature, 440, 1018
Ahnen M. L. et al., 2015, ApJ, 815, L23
Ahnen M. L. et al., 2016a, A&A, 590, A24
Ahnen M. L. et al., 2016b, A&A, 595, A98
Akaike H., 1974, IEEE Trans. Autom. Control, 19, 716
Albert J. et al., 2008, Nucl. Instrum. Meth., A588, 424
Aleksić J. et al., 2016a, Astropart. Phys., 72, 61
Aleksić J. et al., 2016b, Astropart. Phys., 72, 76
Andrews S. K., Driver S. P., Davies L. J. M., Lagos C. d. P., Robotham A. S. G., 2018, MNRAS, 474, 898
Arendt R. G. et al., 1998, ApJ, 508, 74
Atwood W. B. et al., 2009, ApJ, 697, 1071
Barger A. J., Cowie L. L., Richards E. A., 2000, AJ, 119, 2092
Bernstein R. A., 2007, ApJ, 666, 663
Bernstein R. A., Freedman W. L., Madore B. F., 2002, ApJ, 571, 107
Berta S. et al., 2010, A&A, 518, L30
Béthermin M., Dole H., Beelen A., Aussel H., 2010, A&A, 512, A78
Biteau J., Williams D. A., 2015, ApJ, 812, 60
Breiman L., 2001, Mach. Learn., 45, 5
Brun R., Rademakers F., 1997, Nucl. Instrum. Meth., A389, 81
Cambrésy L., Reach W. T., Beichman C. A., Jarrett T. H., 2001, ApJ, 555, 563
Danforth C. W., Keeney B. A., Stocke J. T., Shull J. M., Yao Y., 2010, ApJ, 720, 976
de Angelis A., Roncadelli M., Mansutti O., 2007, Phys. Rev. D, 76, 121301
de Angelis A., Mansutti O., Persic M., Roncadelli M., 2009, MNRAS, 394, L21
de Angelis A., Galanti G., Roncadelli M., 2011, Phys. Rev. D, 84, 105030
Desai A. et al., 2017, ApJ, 850, 73
Domínguez A., Ajello M., 2015, ApJ, 813, L34
Domínguez A., Prada F., 2013, ApJ, 771, L34
Domínguez A., Sánchez-Conde M. A., Prada F., 2011a, J. Cosmol. Astropart. Phys., 11, 20



Downloaded from https://academic.oup.com/mnras/article-abstract/486/3/4233/5427920 by Universita degli Studi di Pisa user on 10 April 2020

Domínguez A. et al., 2011b, MNRAS, 410, 2556
Domínguez A., Finke J. D., Prada F., Primack J. R., Kitaura F. S., Siana B., Paneque D., 2013, ApJ, 770, 77
Driver S. P. et al., 2016, ApJ, 827, 108
Dube R. R., Wickes W. C., Wilkinson D. T., 1979, ApJ, 232, 333
Dwek E., Arendt R. G., 1998, ApJ, 508, L9
Dwek E., Krennrich F., 2013, Astropart. Phys., 43, 112
Elbaz D., Cesarsky C. J., Chanial P., Aussel H., Franceschini A., Fadda D., Chary R. R., 2002, A&A, 384, 848
Fazio G. G. et al., 2004, ApJS, 154, 39
Finkbeiner D. P., Davis M., Schlegel D. J., 2000, ApJ, 544, 81
Finke J. D., Razzaque S., Dermer C. D., 2010, ApJ, 712, 238
Franceschini A., Rodighiero G., 2017, A&A, 603, A34
Franceschini A., Rodighiero G., Vaccari M., 2008, A&A, 487, 837
Frayer D. T. et al., 2006, ApJ, 647, L9
Fruck C. et al., 2013, Proceedings of the 33rd International Cosmic Ray Conference (ICRC2013), Sociedade Brasileira de Fisica, p. 1054
Gardner J. P. et al., 2000, AJ, 119, 486
Ghisellini G., Tavecchio F., Foschini L., Ghirlanda G., 2011, MNRAS, 414, 2674
Gilmore R. C., Somerville R. S., Primack J. R., Domínguez A., 2012, MNRAS, 422, 3189
Gorjian V., Wright E. L., Chary R. R., 2000, ApJ, 536, 550
Gould R. J., Schréder G., 1966, Phys. Rev. Lett., 16, 252
Hatlo M., James F., Mato P., Moneta L., Winkler M., Zsenei A., 2005, IEEE Trans. Nucl. Sci., 52, 2818
Hauser M. G., Dwek E., 2001, ARA&A, 39, 249
Hauser M. G. et al., 1998, ApJ, 508, 25
Heck D., Knapp J., Capdevielle J. N., Schatz G., Thouw T., 1998, CORSIKA: A Monte Carlo Code to Simulate Extensive Air Showers. Forschungszentrum Karlsruhe GmbH, Karlsruhe, Germany
Heitler W., 1984, The Quantum Theory of Radiation, 3rd edn. Dover, New York
Helgason K., Kashlinsky A., 2012, ApJ, 758, L13
Helgason K., Komatsu E., 2017, MNRAS, 467, L36
Helgason K., Cappelluti N., Hasinger G., Kashlinsky A., Ricotti M., 2014, ApJ, 785, 38
Hillas A. M., 1985, 19th International Cosmic Ray Conference, Vol. 3, NASA Goddard Space Flight Center, p. 445
Hooper D., Serpico P. D., 2007, Phys. Rev. Lett., 99, 231102
Inoue Y., Inoue S., Kobayashi M. A. R., Makiya R., Niino Y., Totani T., 2013, ApJ, 768, 197
Inoue Y., Tanaka Y. T., Madejski G. M., Domínguez A., 2014, ApJ, 781, L35
Keenan R. C., Barger A. J., Cowie L. L., Wang W.-H., 2010, ApJ, 723, 40
Khaire V., Srianand R., 2015, ApJ, 805, 33
Kneiske T. M., Dole H., 2010, A&A, 515, A19
Kneiske T. M., Mannheim K., Hartmann D. H., 2002, A&A, 386, 1
Kormendy J., Ho L. C., 2013, ARA&A, 51, 511
Lagache G., Haffner L. M., Reynolds R. J., Tufte S. L., 2000, A&A, 354, 247
Leinert C. et al., 1998, A&AS, 127, 1
Levenson L. R., Wright E. L., 2008, ApJ, 683, 585
Madau P., Dickinson M., 2014, ARA&A, 52, 415
Madau P., Pozzetti L., 2000, MNRAS, 312, L9
Matsumoto T. et al., 2005, ApJ, 626, 31
Matsumoto T., Kim M. G., Pyo J., Tsumura K., 2015, ApJ, 807, 57
Matsuoka Y., Ienaka N., Kawara K., Oyabu S., 2011, ApJ, 736, 119
Matsuura S. et al., 2011, ApJ, 737, 2
Matsuura S. et al., 2017, ApJ, 839, 7
Mattila K., Väisänen P., Lehtinen K., von Appen-Schnur G., Leinert C., 2017, MNRAS, 470, 2152
Mattox J. R. et al., 1996, ApJ, 461, 396
Mazin D., Raue M., 2007, A&A, 471, 439
Metcalfe L. et al., 2003, A&A, 407, 791
Meyer M., Raue M., Mazin D., Horns D., 2012, A&A, 542, A59
Meyer M., Horns D., Raue M., 2013, Phys. Rev. D, 87, 035027
Mirizzi A., Raffelt G. G., Serpico P. D., 2007, Phys. Rev. D, 76, 023001
Moralejo A. et al., 2009, Proceedings of the 31st International Cosmic Ray Conference (ICRC2009), Lodz, Poland(arXiv:0907.0943)
Murase K., Beacom J. F., 2012, J. Cosmol. Astropart. Phys., 10, 043
Nikishov A. I., 1962, Sov. Phys. JETP, 14, 393
Papovich C. et al., 2004, ApJS, 154, 70
Pénin A. et al., 2012, A&A, 543, A123
Pueschel E., 2017, in Proc. Sci., The Extragalactic Background Light: Constraints from TeV Blazar Observations, SISSA, Trieste, PoS#301
Rolke W. A., Lopez A. M., Conrad J., 2005, Nucl. Instrum. Meth. Phys. Res. A, 551, 493
Sanchez D. A., Deil C., 2013, Proceedings of the 33rd International Cosmic Ray Conference (ICRC2013), Sociedade Brasileira de Fis(ica(arXiv:1307.4534)
Sanchez D. A., Fegan S., Giebels B., 2013, A&A, 554, A75
Sánchez-Conde M. A., Paneque D., Bloom E., Prada F., Domínguez A., 2009, Phys. Rev. D, 79, 123511
Shankar F. et al., 2016, MNRAS, 460, 3119
Somerville R. S., Lee K., Ferguson H. C., Gardner J. P., Moustakas L. A., Giavalisco M., 2004, ApJ, 600, L171
Somerville R. S., Gilmore R. C., Primack J. R., Domínguez A., 2012, MNRAS, 423, 1992
Stecker F. W., de Jager O. C., Salamon M. H., 1992, ApJ, 390, L49
Stecker F. W., Scully S. T., Malkan M. A., 2016, ApJ, 827, 6
Takeuchi T. T., Ishii T. T., Hirashita H., Yoshikawa K., Matsuhara H., Kawara K., Okuda H., 2001, PASJ, 53, 37
Tavecchio F., Roncadelli M., Galanti G., Bonnoli G., 2012, Phys. Rev. D, 86, 085036
Tsumura K., Matsumoto T., Matsuura S., Sakon I., Wada T., 2013, PASJ, 65, 121
Urry C. M., Padovani P., 1995, PASP, 107, 803
Voyer E. N., Gardner J. P., Teplitz H. I., Siana B. D., de Mello D. F., 2011, ApJ, 736, 80
Wilks S. S., 1938, Ann. Math. Stat., 9, 60
Wright E. L., Reese E. D., 2000, ApJ, 545, 43
Xu C. K. et al., 2005, ApJ, 619, L11
Zanin R. E. C. J. S., MAGIC, 2013, Proceedings of the 33rd International Cosmic Ray Conference (ICRC2013), Sociedade Brasileira de Fisica. p. 0773
Zemcov M. et al., 2014, Science, 346, 732
Zemcov M., Immel P., Nguyen C., Cooray A., Lisse C. M., Poppe A. R., 2017, Nat. Commun., 8, 15003

## APPENDIX A: MAXIMUM LIKELIHOOD METHOD

In this analysis we have used a joint (i.e. many-spectra) maximum likelihood approach, similar to those used in Abdo et al. (2010), Ackermann et al. (2012), Abramowski et al. (2013), and Abdollahi et al. (2018). The method is implemented in the ROOT-based (Brun & Rademakers 1997) MARS software package (Moralejo et al. 2009; Zanin et al. 2013; Aleksić et al. 2016b), which is the official analysis of the MAGIC collaboration. The joint likelihood $L$ to be maximized is the product of a number of factors, one for every bin ($j$) in estimated energy of every gamma-ray spectrum ($i$) used in the analysis:

$$L(ebl, \theta_1, \theta_2, ..., \theta_{N_{\rm spectra}}, b) = \prod_{i=1}^{N_{\rm spectra}} \prod_{j=1}^{N_{{\rm bins},i}} L_{ij}(ebl, \theta_i, b_{ij}), \qquad \text{(A1)}$$

where each $\theta_i$ is a vector containing the parameters describing the *intrinsic* spectrum $i$ (which are treated as nuisance parameters in the likelihood maximization), and *ebl* is a vector of parameters (or a single parameter) describing the EBL. The parameters $b_{ij}$ are nuisance parameters related to the poissonian background recorded



Downloaded from https://academic.oup.com/mnras/article-abstract/486/3/4233/5427920 by Universita degli Studi di Pisa user on 10 April 2020

together with the gamma-ray signal. Each factor $L_{ij}$ has the form:

$$L_{ij}(ebl, \theta_i) = Poisson(g_{ij}(ebl, \theta_i) + b_{ij},\ N_{\mathrm{on},ij}) \cdot Poisson(b_{ij}/\beta,\ N_{\mathrm{off},ij}). \quad \text{(A2)}$$

Here, $N_{\mathrm{on}}$ and $N_{\mathrm{off}}$ are the numbers of recorded events (after gamma-ray selection cuts) in bins of estimated energy ($j = 1, \ldots, N_{\mathrm{bins},i}$), both around the source direction (ON-source region), $N_{\mathrm{on},ij}$, and in three control regions of identical size (OFF) that contain only background events, $N_{\mathrm{off},ij}$. The Poisson parameters for the signal and the background are, respectively, $g_{ij}$ and $b_{ij}$, which are described in more detail in the next paragraph. The factor $\beta$ is the ratio of ON to OFF exposure, which could be different for each spectrum, but happens to be the same, $\beta = 1/3$, in the analysis presented here – the three OFF sky regions considered for each observation are chosen to have the same acceptance as the ON region. In each spectrum, the $j$ index runs over bins in the range 60 GeV–15 TeV of estimated energy. It is not required that a bin has a significant excess of gamma-like events, but the range is clipped on both ends so that all bins within it contain at least one event in the ON-source region or in the OFF-source region. This results in different fitting ranges for each observation, depending mostly on the range of zenith distance of the observations. In the present analysis of 32 spectra, the total number of considered energy bins is $\sum_{i=1}^{N_{\mathrm{spectra}}} N_{\mathrm{bins},i} = 521$, and the total number of parameters needed to describe the 32 intrinsic spectra varies from 103 to 106, depending on the template EBL model used.

We follow the profile likelihood method described in Rolke, Lopez & Conrad (2005), with the parameter(s) of interest being in our case those that describe the EBL. Each of the $L_{ij}$ terms defined in equation (A2) is the product of two poissonian probabilities: the probability of observing $N_{\mathrm{on},ij}$ events in the ON region, and the probability of observing $N_{\mathrm{off},ij}$ events in the OFF region. The value $g_{ij}$ is the Poisson parameter (mean number) of gammas in the ON-source region for bin $j$ of spectrum $i$, and is obtained by folding the intrinsic source spectrum (given by $\theta_i$) with the EBL absorption (according to the *ebl* parameters), and with the MAGIC response (energy-dependent effective area and energy migration matrix), and multiplying the resulting gamma-ray rate by the observation time. The Poisson parameter of the background in the ON-source region is $b_{ij}$, and it is treated as a nuisance parameter: in each step of the likelihood maximization we look for the value of $b_{ij}$ that maximizes $L_{ij}$, given $g_{ij}$, $\beta$, $N_{\mathrm{on},ij}$, and $N_{\mathrm{off},ij}$. As shown by Rolke et al. (2005), the $b_{ij}$ values can be calculated analytically from the rest of the parameters and the data inputs by solving a quadratic equation.

### A1 Treatment of statistical uncertainties in the MAGIC response

An additional complication arises from the fact that the IRF of the telescopes (with which the gamma-ray spectrum has to be folded) is actually not known with perfect accuracy, since it is obtained from an MC simulation with limited statistics. Therefore, for given parameters ($\theta$, *ebl*), the result of the folding process is not a single value $g_{ij}$ for a given bin, but rather a *range of values*, $g_{ij} \pm \Delta g_{ij}$. In order to account for this, we replace $g_{ij}$ in the expressions above by another nuisance parameter, $g'_{ij}$. Then, assuming that the uncertainty $\Delta g_{ij}$ is Gaussian (this should be the case except in case of very low MC statistics), we add another factor to the likelihood, i.e.

$$L_{ij} = Poisson(g'_{ij} + b_{ij},\ N_{\mathrm{on},ij}) \cdot Poisson(b_{ij}/\beta,\ N_{\mathrm{off},ij}) \cdot Gauss(g'_{ij};\ g_{ij}, \Delta g_{ij}), \quad \text{(A3)}$$

with

$$Gauss(g'_{ij}; g_{ij}, \Delta g_{ij}) = \frac{1}{\sqrt{2\pi}\ \Delta g_{ij}} \mathrm{e}^{-\frac{1}{2}(g'_{ij} - g_{ij})^2/\Delta g_{ij}^2},$$

where $g_{ij}$ and $\Delta g_{ij}$ depend, as in equation (A2), on *ebl* and $\theta_i$. The Gaussian factor above penalizes values of $g'_{ij}$ that are too far from the MC-estimated value $g_{ij}$. This scenario (Gaussian uncertainty in the detector efficiency and poissonian background) is mentioned in Rolke et al. (2005), but not explained in detail. The idea is that now, instead of maximizing each of the $L_{ij}$ terms with respect to $b_{ij}$ alone, we have to look for the values $(b_{ij}, g'_{ij})$ that maximize $L_{ij}$ given $g_{ij}$, $\Delta g_{ij}$, $N_{\mathrm{on},ij}$, $N_{\mathrm{off},ij}$, and $\beta$. It turns out that (dropping the $ij$ indices for clarity), if we fix all other values, the optimal $b$ and $g'$ can also be found analytically, in the general case, by solving a third-degree equation. For the particular cases of $N_{\mathrm{on}} = 0$ or $N_{\mathrm{off}} = 0$, the solution is even simpler, and involves solving a linear and a second-degree equation, respectively – always taking care of forcing $b = 0$ (or $g' = 0$) in the rare cases in which the analytical solution is unphysical, i.e. $b < 0$ ($g' < 0$).

### A2 Use of *Fermi*-LAT constraints

Constraints from contemporaneous *Fermi*-LAT spectra can be incorporated into the method by adding for each spectrum, two additional factors to the likelihood, which correspond to the comparison of the flux and photon index measured at the decorrelation energy of the LAT spectrum, $F_{\mathrm{LAT}} \pm \Delta F_{\mathrm{LAT}}$, $\Gamma_{\mathrm{LAT}} \pm \Delta\Gamma_{\mathrm{LAT}}$ (a 'spectral bow-tie'), and those of the tested spectral function ($F$, $\Gamma$) at the same energy. For these terms we assume the LAT parameter uncertainties to be Gaussian.

$$L_{ij} = L_{ij,\,\mathrm{MAGIC}} \cdot \mathrm{e}^{-\frac{1}{2}\left(\frac{\Gamma - \Gamma_{\mathrm{LAT}}}{\Delta\Gamma_{\mathrm{LAT}}}\right)^2} \cdot \mathrm{e}^{-\frac{1}{2}\left(\frac{F - F_{\mathrm{LAT}}}{\Delta F_{\mathrm{LAT}}}\right)^2}, \quad \text{(A4)}$$

where $L_{ij,\,\mathrm{MAGIC}}$ is given by expression (A3). A 10 per cent systematic uncertainty in the *Fermi*-LAT collection area[6] has been added quadratically to the $F_{\mathrm{LAT}}$ values. With the procedure outlined above, each of the *Fermi*-LAT spectra contributes two additional *data points* (and degrees of freedom) to the fit. A possible improvement over this simplified approach could be achieved through the inclusion in the joint Likelihood of the contributions from each of the *Fermi*-LAT spectral points. It must be remarked however that the points are correlated, and often suffer from low photon statistics, so a rigorous treatment is far from trivial.

### A3 Sources at uncertain redshift

When the redshift of a source is uncertain (which is only the case, in our sample, for PG 1553+113), $z$ is treated also as a nuisance parameter, with flat distribution in the allowed range. This is done by scanning the redshift, in each step of the likelihood maximization process, to maximize the contribution to the joint likelihood of the corresponding spectra.

[1]*Inst. de Astrofísica de Canarias, E-38200 La Laguna, Spain*
[2]*Dpto. Astrofísica, Universidad de La Laguna, E-38206 La Laguna, Tenerife, Spain*
[3]*Università di Udine, INFN Trieste, I-33100 Udine, Italy*

[6]https://fermi.gsfc.nasa.gov/ssc/data/analysis/LAT_caveats.html



Downloaded from https://academic.oup.com/mnras/article-abstract/486/3/4233/5427920 by Universita degli Studi di Pisa user on 10 April 2020

[4]*National Institute for Astrophysics (INAF), I-00136 Rome, Italy*
[5]*ETH Zurich, CH-8093 Zurich, Switzerland*
[6]*Technische Universität Dortmund, D-44221 Dortmund, Germany*
[7]*Croatian Consortium: Department of Physics, University of Rijeka, 51000 Rijeka, Croatia; University of Split – FESB, 21000 Split, Croatia; University of Zagreb – FER, 10000 Zagreb, Croatia; University of Osijek, 31000 Osijek, Croatia; Rudjer Boskovic Institute, 10000 Zagreb, Croatia*
[8]*Saha Institute of Nuclear Physics, HBNI, 1/AF Bidhannagar, Salt Lake, Sector-1, Kolkata 700064, India*
[9]*Centro Brasileiro de Pesquisas Físicas (CBPF), 22290-180 URCA, Rio de Janeiro (RJ), Brazil*
[10]*Unidad de Partículas y Cosmología (UPARCOS), Universidad Complutense, E-28040 Madrid, Spain*
[11]*Department of Astrophysics, University of Łódź, PL-90236 Łódź, Poland*
[12]*Università di Siena and INFN Pisa, I-53100 Siena, Italy*
[13]*Deutsches Elektronen-Synchrotron (DESY), D-15738 Zeuthen, Germany*
[14]*Istituto Nazionale Fisica Nucleare (INFN), I-00044 Frascati (Roma), Italy*
[15]*Max-Planck-Institut für Physik, D-80805 München, Germany*
[16]*Institut de Física d'Altes Energies (IFAE), The Barcelona Institute of Science and Technology (BIST), E-08193 Bellaterra (Barcelona), Spain*
[17]*Università di Padova and INFN, I-35131 Padova, Italy*
[18]*Università di Pisa, and INFN Pisa, I-56126 Pisa, Italy*
[19]*Universität Würzburg, D-97074 Würzburg, Germany*
[20]*Finnish MAGIC Consortium: Tuorla Observatory (Department of Physics and Astronomy) and Finnish Centre of Astronomy with ESO (FINCA), University of Turku, FI-20014 Turku, Finland; Astronomy Division, University of Oulu, FI-90014 Oulu, Finland*
[21]*Departament de Física, CERES-IEEC, Universitat Autònoma de Barcelona, E-08193 Bellaterra, Spain*
[22]*ICCUB, IEEC-UB, Universitat de Barcelona, E-08028 Barcelona, Spain*
[23]*ICRANet-Armenia at NAS RA, 0019 Yerevan, Armenia*
[24]*Japanese MAGIC Consortium: ICRR, The University of Tokyo, 277-8582 Chiba, Japan; Department of Physics, Kyoto University, 606-8502 Kyoto, Japan; Tokai University, 259-1292 Kanagawa, Japan; RIKEN, 351-0198 Saitama, Japan*
[25]*Institute for Nuclear Research and Nuclear Energy, Bulgarian Academy of Sciences, BG-1784 Sofia, Bulgaria*
[26]*Institut für Physik, Humboldt University of Berlin, D-12489 Berlin Germany*
[27]*Dipartimento di Fisica, Università di Trieste, I-34127 Trieste, Italy*
[28]*Port d'Informació Científica (PIC), E-08193 Bellaterra (Barcelona), Spain*
[29]*INAF-Trieste, Department of Physics and Astronomy, University of Bologna, I-40129 Bologna, Italy*

This paper has been typeset from a TEX/LATEX file prepared by the author.

Downloaded from https://academic.oup.com/mnras/article-abstract/486/3/4233/5427920 by Universita degli Studi di Pisa user on 10 April 2020